Design and Acoustic Shielding Prediction of Hybrid Wing-Body Aircraft

by

Leo Wai-Tsun Ng

Bachelor of Applied Science, University of Toronto (2007)

Submitted to the Department of Aeronautics and Astronautics
in partial fulfillment of the requirements for the degree of

Master of Science in Aeronautics and Astronautics

at the

MASSACHUSETTS INSTITUTE OF TECHNOLOGY

June 2009

Author .....
Department of Aeronautics and Astronautics
May 22, 2009

Certified by .....
Zoltán S. Spakovszky
H. N. Slater Associate Professor
Thesis Supervisor

Accepted by .....
David L. Darmofal
Associate Department Head
Chair, Committee on Graduate Students

Design and Acoustic Shielding Prediction of Hybrid Wing-Body Aircraft

by

Leo Wai-Tsun Ng

Submitted to the Department of Aeronautics and Astronautics
on May 22, 2009, in partial fulfillment of the requirements for the degree of
Master of Science in Aeronautics and Astronautics

Abstract

Recent research and developmental efforts in aircraft design have focused on the growing concerns about the environment impact of aviation and the rising costs of fuel. Under NASA's N+2 subsonics fixed-wing project, hybrid-wing-body (HWB) aircraft are investigated with the goal to meet the N+2 noise, fuel burn, and emissions requirements. As part of the N+2 program, this thesis is focused on the design and assessment of an HWB aircraft and the development of a prediction method for turbomachinery noise shielding.

Based on MIT's previous experience in the Silent Aircraft Initiative, the SAX-40 aircraft concept was further developed into the N+2 HWB aircraft. The design effort resulted in two aircraft configurations: the N2A aircraft with conventional podded engines, and the N2B aircraft with a distributed propulsion system embedded in the airframe. The initial performance assessment shows that the N2A and the N2B aircraft can both meet the N+2 fuel burn goal and that the N2A aircraft is 5.7 EPNdB short of the noise goal. Also, the assessment revealed that current noise prediction methods cannot model the advanced propulsion system of the N2B aircraft, requiring the development of noise assessment tools for advanced engine-airframe configurations.

NASA's Aircraft Noise Prediction Program employs the barrier shielding method to predict the airframe shielding of engine noise. However, it is an empirical formulation for straight edges and thus it is not appropriate for the planform shape of an HWB aircraft. At the same time, high fidelity methods such as boundary element methods and ray tracing methods are too computationally expensive if used in the early aircraft design and assessment stage. A compromise is the previously formulated diffraction integral concept based on the Maggi-Rubinowicz representation of Kirchhoff's diffraction theory. The diffraction integral method was implemented and applied to the N2A and the N2B aircraft. A noise reduction of over 20 dB in OASPL due to airframe shielding was predicted, demonstrating the shielding benefit of the HWB configuration. This shielding method is shown to be applicable to any aircraft configuration and planform geometry.

The contributions of this thesis are the design of an HWB aircraft to be used as a platform for the development and evaluation of advanced analysis methods. In addition, a fast and improved-fidelity method for noise shielding prediction was developed, applicable to conventional and advanced airframe configurations such as, for example, the N2A and the N2B HWB aircraft.

Thesis Supervisor: Zoltán S. Spakovszky
Title: H. N. Slater Associate Professor

Acknowledgments

I would like to thank Professor Spakovszky for his guidance and support throughout my graduate studies at MIT. I can always depend on him to take care of his students and provide sound advice. I have learned a lot working with Prof. Spakovszky and it has been a rewarding experience.

I would also like to thank Dr. James Hileman for his help with the project. He is always available to answer questions about the Silent Aircraft Initiative and offer useful suggestions.

I could not have completed the project without my partner, Philip Weed. His willingless to contribute good ideas and help me resolve issues is greatly appreciated.

I have very much enjoyed the company of my officemates and labmates. They are a source of both technical advice as well as much needed distractions throughout the day. Special shoutout to Andreas, Björn, François, Hiten, Jeff, Jon, Shinji, Sho, and Tanya for making the GTL a great place to work.

This work is funded by NASA's N+2 Subsonics Fixed-Wing program. I would like to thank Casey Burley, Doug Nark, and Stuart Pope at NASA Langley for their help with ANOPP and for providing the FSC noise shielding data.

Finally, to all my friends at MIT, thanks for making the past two years some of the best experiences of my life.

Contents

List of Figures

List of Tables

Nomenclature

Abbreviations

ANOPP	Aircraft NOise Prediction Program
BEM	Boundary Element Method
BL	Boundary Layer
BWB	Blended-Wing-Body
CAEP	Committee on Aviation Environmental Protection
CFD	Computational Fluid Dynamics
CMI	Cambridge-MIT Institute
EPNL	Effective Perceived Noise Level (EPNdB)
FAR	Federal Aviation Regulations
FSC	NASA's Fast Scattering Code for noise shielding prediction
GRC	NASA Glenn Research Center
HWB	Hybrid-Wing-Body
ICAO	International Civil Aviation Organization
ISA	International Standard Atmosphere
LaRC	NASA Langley Research Center
LTO	Landing and Take-Off
MTOW	Maximum Take-Off Weight
N2A	N+2 project hybrid-wing-body aircraft with conventional podded engines
N2B	N+2 project hybrid-wing-body aircraft with embedded propulsion system
NPSS	NASA's Numerical Propulsion Simulation software
OEW	Operational Empty Weight

PNLT	Tone-corrected Perceived Noise Level (dB)
RANS	Reynolds Average Navier-Stokes
RSM	Response Surface Model
SAI	Silent Aircraft Initiative
SAX	Silent Aircraft eXperimental
SPL	Sound Pressure Level
UCI	University of California at Irvine

Roman Symbols

A	area of aperture (m^2)
A	surface area (m^2)
A	wing area (m^2)
a	reference or characteristic length (m)
A_0	area of control surface excluding aperture (m^2)
c_i	coefficients for structure weight response surface model for i from 1 to 5
C_D	total drag coefficient
C_{Df}	friction drag coefficient
C_{Di}	induced drag coefficient
C_{Dp}	pressure drag coefficient
C_L	lift coefficient
D	engine fan diameter (m)
$h_n^{(1)}$	spherical Hankel functions of the 1^{st} kind
I_1	non-singular part of the integrand
I_2	singular part of the integrand
j_n	spherical Bessel functions
k	wave number (m^{-1})
ML/D	flight Mach number times lift-to-drag ratio
N	number of grid points

p_d	diffracted acoustic pressure (Pa)
$p_{d,A}$	acoustic pressure diffracted through aperture (Pa)
$p_{d,O}$	acoustic pressure diffracted around shielding object (Pa)
p_i	incident acoustic pressure without diffraction (Pa)
P_n	Legendre polynomials
$\vec{r}$	vector from origin to observer (m)
r	magnitude of $\vec{r}$ (m)
R	distance between source and observer (m)
s	distance along the contour of integration (m)
T	thrust (N)
V_2	reference take-off speed according to FAR 25.107 (knots)
V_{ref}	reference landing speed according to FAR 25.125 (knots)
W_{fuel}	fuel weight (lb)
W_{pay}	payload weight (lb)
W_{prop}	propulsion system weight (lb)
W_{struct}	structure weight (lb)
x, y, z	coordinate system relative to aircraft: x = aft, y = starboard, z = up
$\vec{x}$	coordinates of observer (m)
$\vec{y}$	coordinates of a point on the contour of integration (m)
$\vec{z}$	coordinates of source (m)

Greek Symbols

$\vec{\rho}$	vector from origin to source
ρ	magnitude of $\vec{\rho}$

Chapter 1

Introduction

Although continuing growth in commercial aviation is projected, air traffic is being increasingly restricted by congestion at major airports. This has created demand for a step change in noise reduction for airlines to expand into regional airports and for cargo operators to expand into the night curfew [3]. At the same time, fuel costs and environmental concerns are causing aircraft manufacturers to focus on fuel efficiency in new aircraft designs. In response to these factors, considerable research has been done to reduce aircraft noise and fuel burn.

One such project, funded by the UK government, is the Cambridge-MIT (CMI) Silent Aircraft Initiative (SAI). Its goal was to design an aircraft whose noise outside the airport boundaries is less than the background noise level in a typical urban environment. The result was the Silent Aircraft eXperimental (SAX-40) hybrid-wing-body aircraft concept along with advanced operational procedures that was calculated to achieve 61 dBA with a 25% reduction in fuel burn [4]. The SAX-40 prototype demonstrated that a hybrid-wing-body (HWB) configuration—in which the outer wings smoothly transition to the lifting fuselage—has the potential for both noise and fuel burn reduction. In other words, it is not always necessary to trade fuel efficiency for low noise or vice versa.

Similarly, current NASA funded research focuses on reductions in noise, fuel burn, and emissions of future aircraft in the 2020 time frame. The present work is part of the NASA N+2 project, where N+2 denotes the second generation of aircraft beyond the

Table 1.1: NASA goals for the next two generations of aircraft

	N+1 Advanced Conventional 2012–2014	N+2 HWB 2018–2020
Noise (cumulative below FAR 36 stage 3)	−42 dB	−52 dB
Emissions (LTO NOx below CAEP/2)	−70%	−80%
Fuel Burn (relative to equivalent current aircraft)	−15%	−25%

current fleet. The NASA goals are summarized in Table 1.1. The main contributions of this thesis include airframe design, aircraft noise assessment, and an improved noise shielding prediction method.

1.1 NASA N+2 Subsonic Fixed-Wing Project

The research described here is part of a broader collaboration between Boeing Phantom Works, the NASA Glenn Research Center (GRC), the NASA Langley Research Center (LaRC), the University of California at Irvine (UCI), and the Gas Turbine Laboratory at the Massachusetts Institute of Technology (MIT) funded by NASA's N+2 Subsonic Fixed Wing project. The main objective is to develop advanced methodologies for the design of a quiet, fuel-efficient aircraft that meets the NASA N+2 goals. The project is divided into two phases:

Phase I

- Define a non-proprietary HWB aircraft configuration to be used as a platform for assessment of methods and technologies developed during the project.
- Perform an initial noise and fuel burn assessment of the aircraft.
- Begin planning the aero-acoustic and aerodynamic wind tunnel test.

Phase II

- Improve prediction methods for the analysis of unconventional HWB aircraft.
- Refine the candidate HWB aircraft to meet the N+2 goals.
- Fabricate the HWB aircraft model for the wind tunnel test.
- Validate prediction methods against aero-acoustic and aerodynamic test data.

The work of this thesis spans Phase I and the beginning of Phase II of the N+2 project. MIT's reponsibility includes the initial airframe design, airframe noise prediction, improvements to noise prediction methods, and the overall noise assessment of the aircraft. The engines, in terms of both performance and noise aspects, are investigated by NASA GRC. However, jet noise is handled by UCI. Boeing's role is to develop the final aircraft configuration by integrating the engines with the airframe.

1.2 Previous Work

The hybrid-wing-body aircraft concept has been explored for both commercial use and military use in the past several decades. Many variations of this configuration exist under different names, but a well-known example is Boeing's Blended-Wing-Body (BWB) concept that began circa 1993 [5]. The initial NASA-sponsored study of an 800 passenger, 7000 nm design found 15% reduction in take-off weight and 27% less fuel burn relative to conventional aircraft of that time. Further refinement of the BWB configuration by Boeing resulted in additional performance gains. A chronology of the development of the BWB was given by Leibeck in [6].

Due to integration and coupling of the fuselage, wings, and engines, the BWB aircraft configuration provided an opportunity to to pursue multidisciplinary design and optimization during the development process [7]. Boeing's WingMOD software, originally used to design the wings and tails of conventional aircraft, was adapted to analyze the BWB aircraft. It brings together the aerodynamic, structure, weight,

control, and stability aspects of the analysis to optimize the performance of the BWB aircraft [8].

Most past investigations into the HWB-type configurations focused on its fuel burn and performance rather than noise. Meanwhile, there were many advances in noise reduction technologies for conventional aircraft, including continuous mold-line for high lift devices [9, 10], low-noise landing gears [11, 12], and wing trailing edge brushes [13]. The previously mentioned Silent Aircraft Initiative, launched in 2003, investigated the HWB concept as a way to reduce noise. It was found that, in addition to other low-noise technologies incorporated in the design, the HWB airframe provides a significant amount of noise shielding [14]. Therefore, part of the work during the SAI involved developing a prediction method for noise shielding. Further discussion on the previous work during the SAI as well as on various prediction methods for noise shielding are deferred to Section 2.1 and Secton 4.1, respectively.

1.3 Thesis Objectives

Leveraging off MIT's previous experience in the SAI, the N+2 aircraft was designed using the SAX-40 airframe as a starting point. To ensure a consistent noise comparison with the current fleet, the N+2 aircraft noise was estimated according to the Federal Aviation Regulations Part 36 (FAR 36) using NASA LaRC's Aircraft NOise Prediction Program (ANOPP). However, ANOPP was developed primarily for conventional aircraft and there are challenges in modeling certain aspects of advanced configurations such as an HWB type airframe. One particular shortcoming is the prediction of turbomachinery noise shielding, which is an important part of the overall noise reduction strategy. An accurate noise assessment therefore requires improvements to ANOPP, one being the establishment of a noise shielding prediction method for advanced airframe configurations.

ANOPP currently employs the barrier shielding method developed by Beranek [15] and Maekawa [16]. It is based on an empirical correlation of noise attenuation to Fresnel's number for a semi-infinite rectangular screen, i.e. a straight edge. This

is incompatible with the planform shape of an HWB airframe and thus an alternate shielding prediction method is required. However, high fidelity methods such as boundary element methods, equivalent source methods, and ray tracing methods are too computationally expensive for a FAR 36 noise assessment, especially if a large number of aircraft configurations is to be explored. Therefore, a faster, improved-fidelity method (relative to barrier shielding) is proposed.

Based on the diffraction integral method previously formulated by Lummer [17], a noise shielding prediction method was developed for unconventional planform configurations such as the HWB airframe. The method is relatively fast and is able to handle high frequencies necessary in a FAR 36 noise assessment. It also retains the simplicity of the current ANOPP shielding method in that only an outline of the shielding geometry is required. This makes the method useful during the initial aircraft design phase when the full 3-D geoemtry is not yet available. When the aircraft configuration is finalized, a more accurate shielding outline can be determined to improve the shielding prediction.

Based on the above, the thesis objectives in support of the N+2 project can be summarized as follows. The objectives are to:

1. Modify and re-design the SAX-40 airframe to meet the N+2 project requirements.

2. Estimate the aircraft noise and evaluate it against the N+2 noise goal.

3. Improve the fidelity of ANOPP's turbomachinery noise shielding prediction[1] with the diffraction integral method.

1.4 Thesis Contributions

The preliminary design and assessment of an HWB aircraft to meet NASA's N+2 goals were conducted. ANOPP modules that are not able to model the advanced aircraft configuration were identified for further development. In particular, the diffraction

[1] Jet noise shielding prediction is handled by UCI

integral method for turbomachinery noise shielding prediction was implemented as an improvement to ANOPP's barrier shielding method. Application of the diffraction integral method to the N+2 aircraft showed that the HWB planform can provide over 20 dB of noise attenuation, demonstrating the low-noise benefit of this aircraft configuration.

The three major topics, aircraft design, noise assessment, and shielding prediction, are described in the following three chapters, respectively.

Chapter 2

N+2 Aircraft Definition

An HWB type airframe configuration was chosen because of its advantages in fuel efficiency and low noise. As demonstrated by the Silent Aircraft Initiative SAX-40 aircraft, the HWB configuration provides a lifting center body to increase aerodynamic efficiency and a large planform for engine noise shielding. With the non-proprietary nature of the SAX-40 geometry and the analysis tools already in place, the SAX-40 was a good starting point for the design of the N+2 aircraft.

Boeing's mission analysis indicated that a cargo freighter would be the appropriate role for a HWB aircraft in the 2020 time frame. Thus, the objective was to convert the SAX-40 passenger aircraft into a freighter, designated here as the SAX-40F. Table 2.1 compares the mission profile of the SAX-40 and the SAX-40F. The payload weight is doubled and the range is extended by 20%.

This chapters describes the development of the SAX-40F and the methods used in its analysis. SAX-40F was further refined by Boeing to produce two aircraft configurations for the N+2 project: the N2A and the N2B aircraft.

Table 2.1: Mission comparison between SAX-40F and SAX-40

	SAX-40F	SAX-40
Payload Type	cargo	215 passengers
Payload Weight	103,000 lb	51,600 lb
Range	6000 nm	5000 nm

Figure 2-1: The Silent Aircraft Initiative SAX-40 hybrid-wing-body aircraft [4]

2.1 Cambridge-MIT SAX-40

The SAX-40, shown in Figure 2-1, was designed with key technologies that enabled it to meet the background noise goal outside the airport boundary while burning 25% less fuel than current aircraft [4].

The center body and the outer wing profiles were tailored for elliptical lift distribution at cruise to achieve $ML/D = 20$ [4]. For balance, the noise section was cambered to generate lift in the forward position, allowing the use of supercritical outer wing airfoils and less sweep [18]. A distributed propulsion system in which each of the three cores powers three fans results in a high bypass ratio and hence high propulsive efficiency. Furthermore, the engine clusters were partially embedded into the airframe suction surface so that the engines ingest the airframe boundary layer to reduce lost power in the wake [19].

Extensive acoustic liners were employed along the engine ducts to damp out turbomachinery noise. In addition, the top-mounted engines benefit from noise shielding provided by the large planform. Thrust vectoring variable area exhaust nozzles were used during take-off to optimize the thrust and climb gradient for low noise and eliminate the need for noisy elevon deflections [20]. On approach, continuous mold-line technology reduces elevon side edge noise and undercarraige fairings reduce shed vortex noise from the struts and the wheels.

The technologies incorporated into the SAX-40 were carried forward to the SAX-40F. However, advanced operational procedures such as thrust vectoring and variable

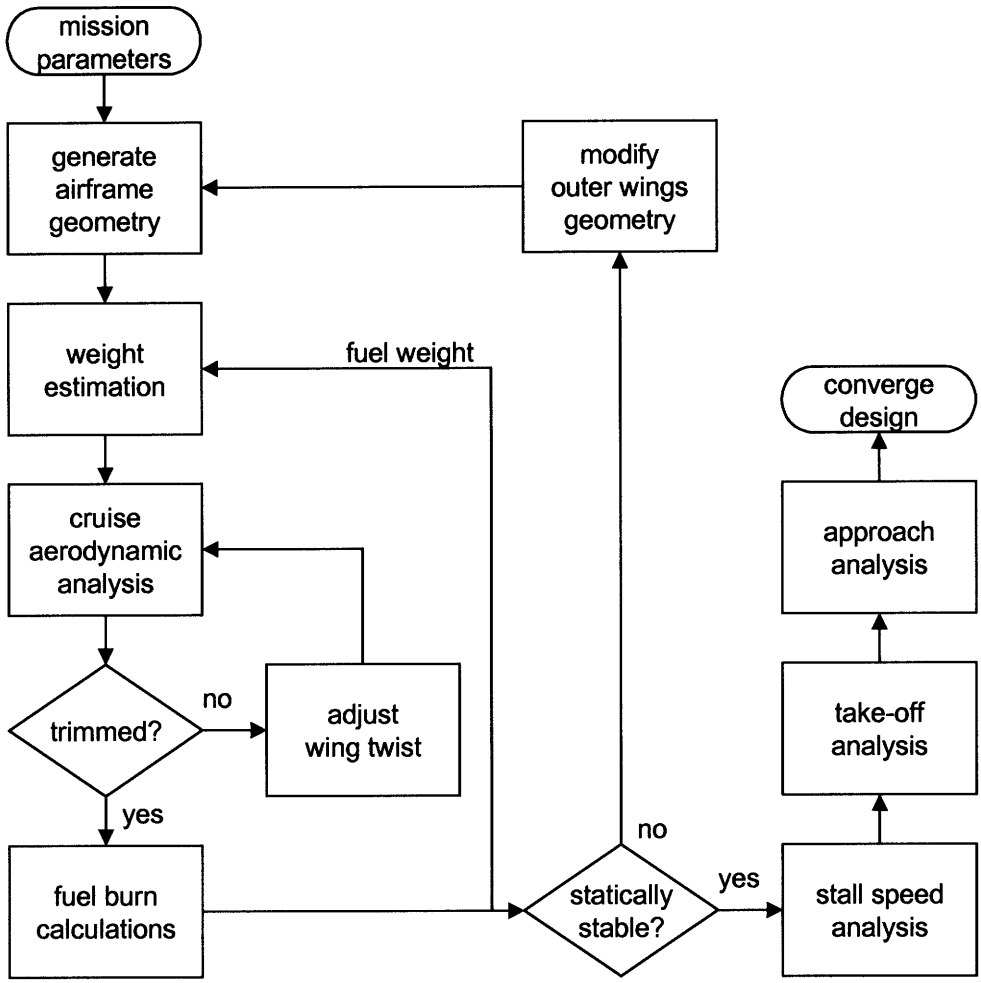

Figure 2-2: Flowchart of the performance analysis framework

area nozzles were not used in order to remain compliant with the current landing and take-off (LTO) procedures specified by the Federal Aviation Administration.

2.1.1 Aircraft Design and Analysis Framework

For rapid design turnaround, the aircraft analysis framework integrates the quasi 3-D aerodynamic method with performance calculations that include weights and fuel burn estimation. By avoiding costly 3-D computational fluid dynamics (CFD), the framework is able to quickly explore and analyze the design space. It was originally developed during the SAI [4] and was adapted here to the freighter mission profile. The overall procedure, illustrated in Figure 2-2, is explained below followed by a description of the quasi 3-D aerodynamic design method in Section 2.1.2.

The analysis begins with the creation of the airframe geometry, i.e. the airfoil stack, based on input parameters. The weight estimation includes models for structure weight, propulsion system weight, undercarriage weight, and fixed equipment weight [21]. The main algorithm loop then produces the cruise aerodynamic data using the quasi 3-D aerodynamic design method and calculates the fuel weight. Fuel weight is iteratively fed back into the weight model to update the weight estimation until the system converges. A stability check is performed and the outer wing geometry is adjusted until the static margin is satisfactory. Finally, a low-speed analysis is performed on the converged and statically stable system.

In order to use this framework to analyze the SAX-40F, the weight model must be updated to reflect a freighter, rather than a passenger, configuration. In addition to changing the fixed equipment weight[1], the propulsion system weight was scaled up and the structure weight model was updated. They latter two are briefly discussed in Sections 2.1.3 and 2.1.4 following the description of the quasi 3-D aerodynamic design method.

2.1.2 Quasi 3-D Aerodynamic Design Method

The challenge in the aerodynamic analysis of an HWB is capturing the 3-D effect of the lifting center body as well as estimating the parasitic drag. The quasi 3-D aerodynamic design method avoids a full 3-D viscous CFD calculation by combining 2-D inviscid vortex lattice method (AVL[2]), 2-D viscous airfoil analysis (MSES[3]), and Hoerner's empirical drag formulas [22]. The vortex lattice method calculates the spanwise lift, induced drag, and moment distributions used by the 2-D viscous airfoil analysis to obtain the viscous drag, pressure drag, and transonic wave drag of each outer wing section. However, the 2-D viscous airfoil analysis cannot be used at the center body due to the 3-D flow field. Instead, Hoerner's correlations for bodies of revolution were used to estimate the center body's contribution to the viscous drag

[1]For example, removing passenger seats, galleys, in-flight entertainment systems, meals, etc.
[2]Athena Vortex Lattice by Mark Drela.
[3]Multi-Element Airfoil Design/Analysis Software by Mark Drela.

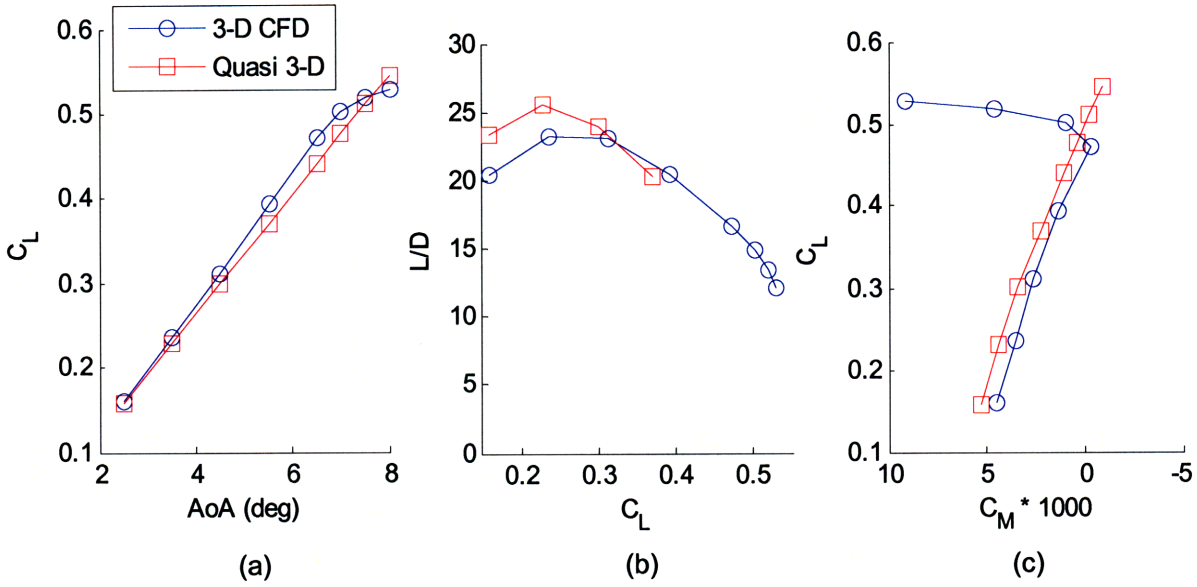

Figure 2-3: SAX-40F comparison of (a) lift curve, (b) lift-to-drag curve, and (c) moment curve between the quasi 3-D aerodynamic design method and 3-D viscous CFD (winglets not included)

and pressure drag.

The quasi 3-D aerodynamic design method compared well with the 3-D RANS analysis conducted by Boeing on the SAX-40F airframe. Figure 2-3 shows good agreement in lift and moment until the stall point and, more importantly, suggests that the 2-D viscous airfoil analysis and the empirical drag formulas produce reasonable drag estimates. To see if the important flow features are adequately captured, pressure coefficient contours of the SAX-40 airframe are compared with 3-D viscous CFD in Figure 2-4. The vortex lattice method produced the expected 3-D effect at the center body and the 2-D viscous airfoil analysis compensated for the inability of the vortex lattice method to predict the shocks on the outer wings.

2.1.3 Propulsion Weight Scaling

The heavier payload and longer range of SAX-40F relative to SAX-40 necessitate a larger engine that must be reflected in the propulsion system weight. This was accomplished by scaling the SAX-40 engine component weights with the top-of-climb

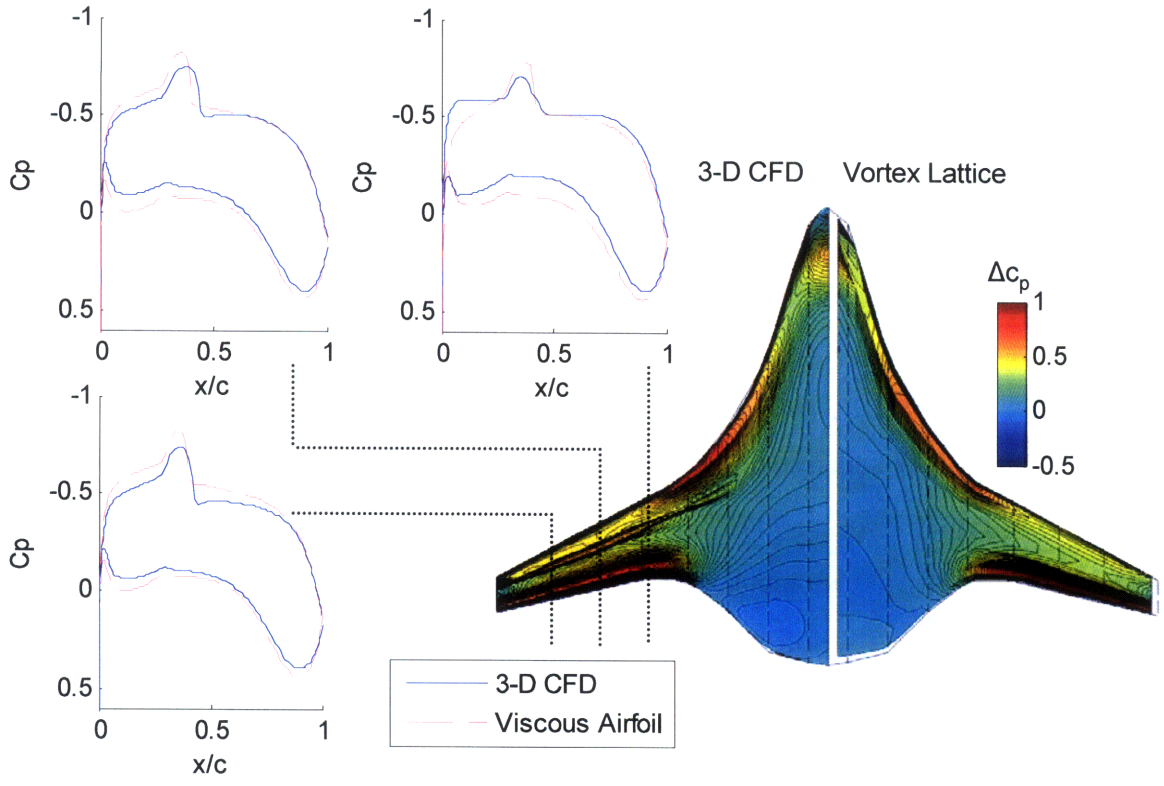

Figure 2-4: SAX-40F comparison of pressure coefficient between the quasi 3-D aerodynamic design method and 3-D viscous CFD (winglets not included)

thrust[4], T. The assumptions made are listed below:

- Since thrust is proportional to mass flow, fan diameter, D, scales with $\sqrt{T}$.
- Gas generator weight scales with $D^{2.4}$ [21].
- Modeling the shafts of the transmission system as torsion rods, transmission system weight scales with T or D^2.
- Oil system weight is assumed constant.
- Nacelle weight is calculated as a function of D based on Raymer's military inlet duct formula [23].
- Nozzle weight is calculated as a function of D based on Boeing's formula [24].
- Engine support weight assumed to scale with the sum of all of the above.

Incorporating the above changes into the overall SAX-40F analysis framework resulted in a 36% increase in propulsion system weight over SAX-40, corresponding to 32% increase in top-of-climb thrust.

2.1.4 Structure Weight Response Surface Model

The structure weight, W_{struct}, was estimated using a response surface model (RSM) that must be updated before it can be applied to the SAX-40F. The RSM is a least-squares fit of structure weight to a set of parameters. However, the SAX-40F design point was anticipated to lie beyond the range of the parameters used to generate the SAX-40 RSM. Therefore, a new SAX-40F RSM was created based on a more appropriate range of parameters.

The proposed set of parameters for the SAX-40F RSM are wing area, A, wing span, b, payload, W_{pay}, fuel weight, W_{fuel}, and propulsion system weight, W_{prop}. To generate the data needed for the correlation, these five parameters were perturbed several percentages above and below their anticipated design value and WingMOD

[4]The SAX-40 engine was sized at top of climb.

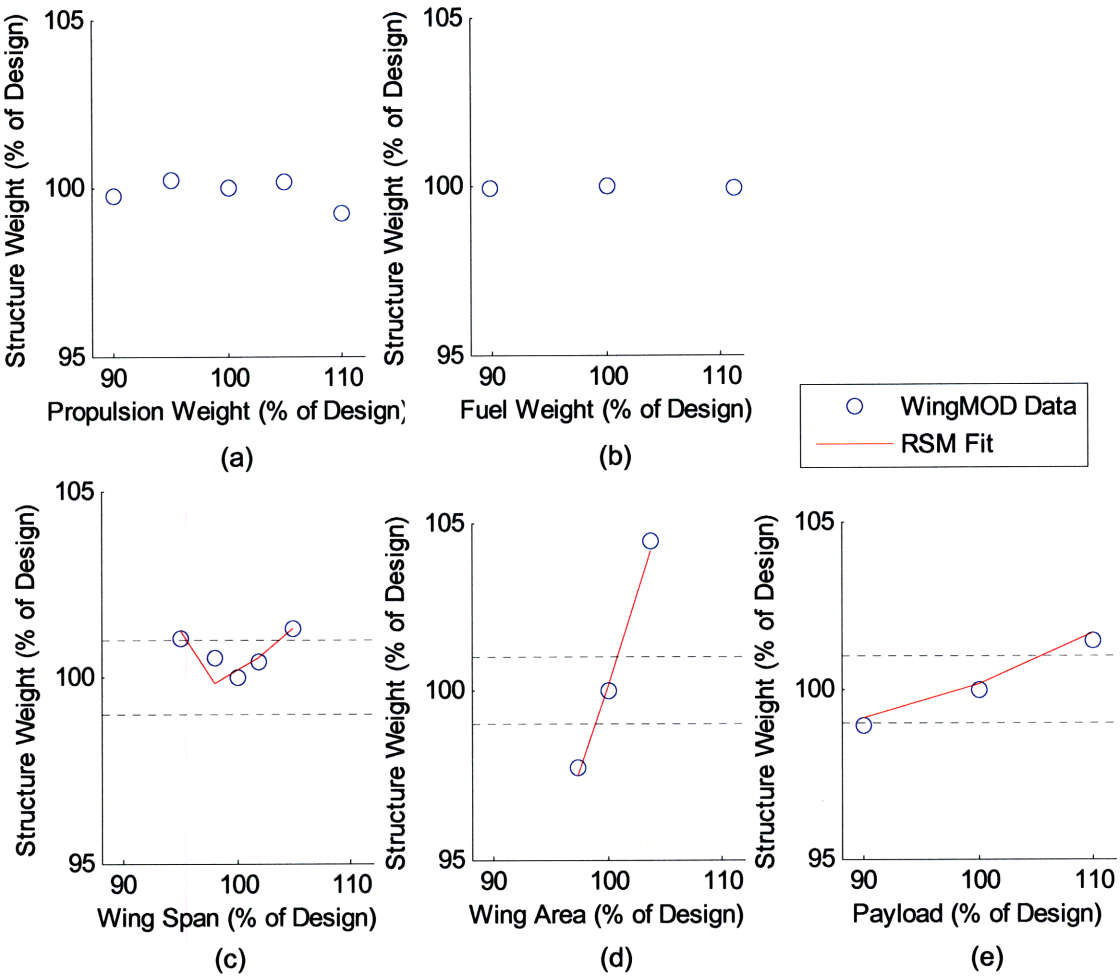

Figure 2-5: Variation in structure weight with respect to (a) propulsion system weight, (b) fuel weight, (c) wing span, (d) wing area, and (e) payload

[25] was used to calculate the structure weight resulting from each perturbation. WingMOD is Boeing's multidisciplinary design and optimization code that considers the aerodynamics, performance, structural loads, weights, stability, and control aspects of a blended wing body aircraft. It was used here, even though the aircraft design it creates is different from the SAX-40 or the SAX-40F, because of a lack of available data on the structure weight of HWB[5].

The variation of structure weight with the five parameters generated by WingMOD are plotted in Figure 2-5. The data in (a) and (b) shows that perturbations in propulsion system weight and fuel weight produce less than 1% change in structure

[5]WingMOD was also used to generate the structure weight RSM for SAX-40 [21].

weight, represented by the dotted horizontal line. Therefore, it is assumed that structure weight is independent of propulsion system weight and fuel weight. Furthermore, the results in Figure 2-5 (c) suggest a quadratic dependence of structure weight on the wing span. Based on these considerations, the following form of the RSM for the SAX-40F was considered:

$$W_{struct} = c_1 A + c_2 W_{pay} + c_3 b + c_4 b^2 + c_5 \tag{2.1}$$

$$c_1 = 13.106 \text{ lb/ft}^2 \quad c_2 = 0.11283 \text{ lb/lb} \quad c_3 = -4113.0 \text{ lb/ft}$$

$$c_4 = 9.6717 \text{ lb/ft}^2 \quad c_5 = 421970 \text{ lb}$$

The coefficients c_1 to c_5 were found by a least-squares fit with a r.m.s. error of 0.3% and comparison between the RSM and WingMOD data are shown in Figure 2-5 (c), (d), and (e). Replacing the SAX-40 RSM with the new SAX-40F RSM in the SAX-40F analysis resulted in a 0.4% increase in structure weight. While the difference is small, it was important to capture the correct functional dependence for structure weight as the SAX-40F design was optimized.

2.2 Aircraft Definition

Using the modified analysis framework, the SAX-40 design evolved into the SAX-40F for the new freighter mission. Changes to the SAX-40 are:

- Wing span reduced from 67.5 m to 64.5 m to operate in ICAO Annex 14 Code E airports.
- Rear spar across center body moved aft by 84 cm on recommendation from Boeing to accommodate more cargo.
- Fuel tanks moved from the sides of the center body to the outer wings, similar to the fuel tanks on conventional aircraft.

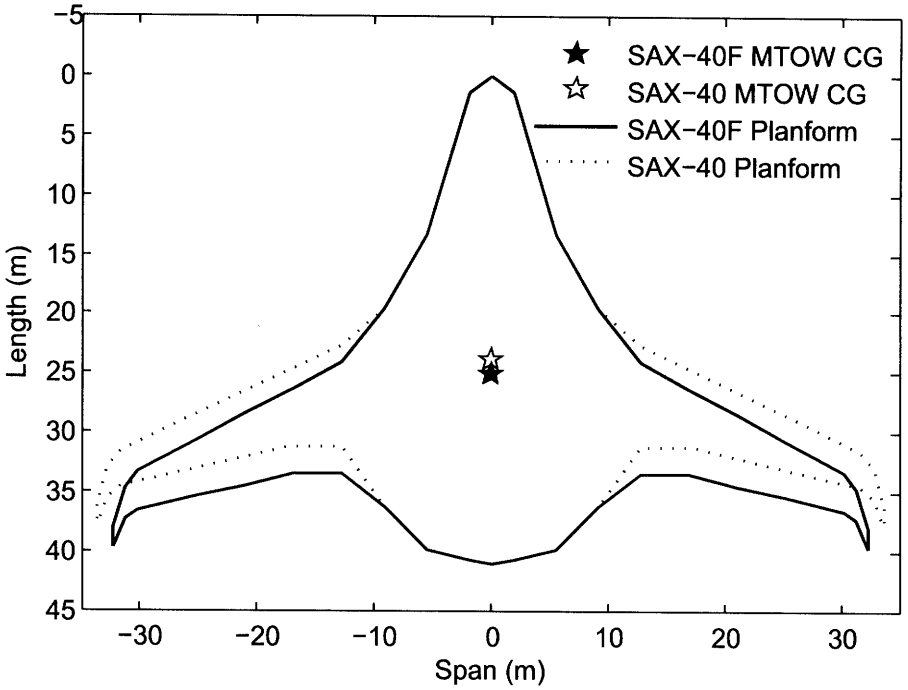

Figure 2-6: Comparison between the SAX-40F and the SAX-40 planform

- Outer wing geometry such as sweep, twist, chord, and position adjusted to maintain static margin as propulsion system weight increased.

The exterior of the center body and all the airfoil shapes remain unchanged from the SAX-40. The adjustments made to the outer wings can be seen in Figure 2-6. The more rearward position of the SAX-40F center of gravity required more sweep on the outer wings in order to move the neutral point rearward.

2.2.1 Comparison between the SAX-40 and the SAX-40F

Performance analysis showed that despite the changes to the outer wings, the SAX-40F was able to maintain the aerodynamic advantages of the SAX-40 design. Comparison between the SAX-40F and the SAX-40 in Figure 2-7 (a) indicates a similarly high lift-to-drag ratio for both aircraft. The aerodynamic efficiency can be attributed to the HWB type design: the lifting center body and the outer wings were contoured to produce an optimal, near-elliptical lift distribution, as shown in Figure 2-7 (b). For a breakdown of the airframe drag and other aerodynamic data generated by the

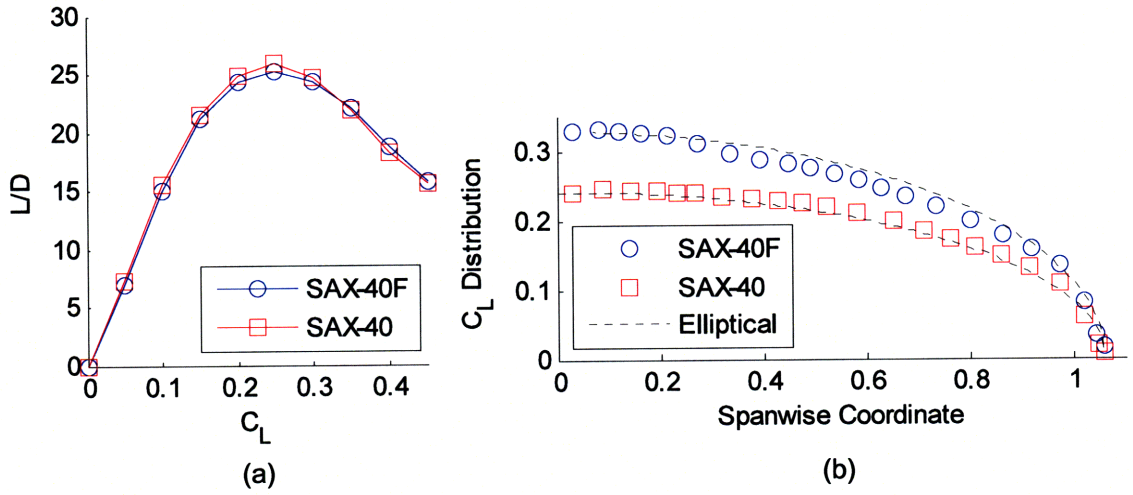

Figure 2-7: Comparison of (a) lift-to-drag ratio and (b) spanwise lift distribution between the SAX-40F and the SAX-40

quasi 3-D aerydanamic design method for the start of cruise, the reader may refer to Table 2.2.

The weight buildup of the SAX-40F and the SAX-40 is tabulated in Table 2.3. While the OEW increased by only 3%, payload and fuel weight increased by 100% and 50%, respectively, resulting in an overall MTOW increase of 28%. The relatively modest increase in OEW is due to the much lighter fixed equipment weight for a freighter configuration.

The SAX-40F airframe geometry and performance data were delivered to Boeing for further analysis and refinement. Combining the basic airframe design of the SAX-40F and the engine design from NASA GRC, the N+2 aircraft configuration was defined.

2.2.2 N+2 Hybrid-Wing-Body Configuration: N2A and N2B

Based on the SAX-40F airframe, Boeing refined the design and created the N2A and the N2B HWB aircraft as a platform for the assessment of the tools and methods to be developed under the N+2 project. The N2A aircraft, illustrated in Figure 2-8 (a), has two conventional 1.6 FPR pod-mounted engines designed by NASA GRC, two vertical tails, and no winglets. The hypothesis is that the vertical tails provide

Table 2.2: Aerodynamic data for the SAX-40F and the SAX-40 at the start of cruise

	SAX-40F	SAX-40
Wing Area (m^2)	845	836
Wing Span (m)	64.5	67.5
Angle of Attack (deg)	3.8	2.7
C_L	0.2617	0.2064
ML/D	20.1	20.1
Static Margin (%)	5.5	5.9
C_D	0.0104	0.0082
C_{Di}	0.0043	0.0024
C_{Dp} center body	0.0004	0.0004
C_{Dp} outer wings	0.0007	0.0005
C_{Df} center body	0.0026	0.0027
C_{Df} outer wings	0.0019	0.0018
C_D wave	0.0002	0.0001
C_D nacelles	0.0004	0.0004

Table 2.3: Weight buildup (in lb) of the SAX-40F and the SAX-40

	SAX-40F	SAX-40
Maximum Take-Off Weight	426,092	332,563
Payload	103,218	51,600
Fuel with Reserves	109,817	73,306
Operational Empty Weight	213,057	207,657
Structure	113,209	104,872
Propulsion	49,876	36,809
Undercarriage	18,499	14,758
Fixed Equipment	31,474	51,219

Figure 2-8: Rendering of the SAX-40F based N2A and N2B HWB aircraft [picture courtesy of D. Odle, Boeing]

additional lateral engine noise shielding[6]. The N2B aircraft, illustrated in Figure 2-8 (b), has three embedded 1.5 FPR engine clusters of nine fans powered by three cores. The configuration is similar to the SAX-40F aircraft except that the engines were redesigned by NASA GRC. The intent of the N2B embedded engine design is to investigate the risk and benefits of more advanced technologies.

Boeing's analysis indicated that the fuel efficiency in terms of payload-range per pound of fuel of the N2A and N2B are 2.47 ton·nm/lb and 2.37 ton·nm/lb, respectively. This represents over 25% reduction in fuel burn compared to the B767 freighter, thus meeting the N+2 fuel burn goal. With the aircraft configuration defined, the noise assessment for the aircraft could begin.

[6]This is demonstrated in Chapter 4.

Chapter 3

N+2 Noise Assessment

The landing and take-off (LTO) noise of the N2A and the N2B aircraft were estimated using the NASA Aircraft Noise Prediction Program (ANOPP) to both evaluate the aircraft against the N+2 noise goal and to assess ANOPP's applicability to hybrid-wing-body type aircraft. ANOPP has been continually updated by NASA LaRC to include the most recent semi-empirical noise estimation methods. However, many of the methods are based on correlations of noise data from conventional aircraft configurations and may not be suitable for an HWB type aircraft configuration. Therefore, as a first step towards a complete noise assessment, the current version of ANOPP was used to identify shortcomings in ANOPP's modules when estimating the N2A and the N2B aircraft noise. Much of the work is captured in [26] and as such, only a summary is presented in this chapter.

3.1 FAR 36 Requirements for Noise Certification

In order to make a fair comparison between the N2A and the N2B against current aircraft, noise measurement rules in the Federal Aviation Regulations (FAR) Part 36 were applied to the N2A and the N2B aircraft. Special low-noise operational procedures, such as those used in the SAI, were not considered.

FAR 36 requires LTO noise to be measured at three locations relative to the airport runway: approach, lateral, and flyover [27, 28]. The conditions are summarized below:

Approach

- Observer located along centerline 2000 m before runway threshold.
- Maintain $-3\,^{\circ}\mathrm{C}$ glide angle, corresponding to 120 m altitude at the microphone.
- Maintain true airspeed $V_{ref} + 10$ knots.
- Maximum landing weight.
- Noisiest configuration, e.g. landing gear extended, flaps deployed, etc.

Lateral

- Observer located 450 m to the side of the centerline where noise after lift-off is maximum.
- Maximum noise can be assumed to occur when aircraft is at 300 m altitude.
- Mantain true airspeed between $V_2 + 10$ knots and $V_2 + 20$ knots.
- Full take-off engine power with no thrust cutback.
- Maximum take-off weight.

Flyover

- Observer located along centerline 6500 m after brakes-off.
- Mantain true airspeed between $V_2 + 10$ knots and $V_2 + 20$ knots.
- Full take-off engine power until at least 300 m altitude, typically 900 m to 1200 m before observer.
- Cutback thrust level must maintain 4% climb gradient or level flight with one engine inoperative, whichever is greater.
- Maximum take-off weight.

All noise measurements are made at ISA + 10 °C day, 70% humidity, zero wind, and sea level conditions. The metric used for FAR 36 noise certification is the effective perceived noise level (EPNL). It is calculated from the intantaneous perceived noise levels, based on noy, and corrected for tones and duration of the sound. The result is a single number, in EPNdB, representing the perceived aircraft noise at each of the approach, lateral, and flyover observer locations. The sum of the three[1] is the benchmark for the N+2 noise goal.

3.2 NASA Aircraft Noise Prediction Program

ANOPP is a fast noise estimation tool useful for calculating EPNL at FAR 36 conditions. It treats each noise generating mechanism on the aircraft as a compact source with directivity. In the current version of ANOPP, all noise sources are assumed to originate from the same location on the aircraft, but the next version of ANOPP is planned to include the actual location of each noise source. The noise sources are propagated at every time step to the observer as the aircraft travels along its LTO trajectory. The propagation includes the effect of spherical spreading, atmospheric absorption, ground reflection and attenuation, and retarded time. The perceived noise at the observer is then summed and converted into EPNL.

ANOPP is organized into many interchangeable modules. There is at least one module for estimating the amplitude and directivity of each noise source. Most of the noise estimation modules are based on empirical wind tunnel or flight test data of past aircraft. As such, the modules may produce erroneous results for aircraft, like the N2A and the N2B, that is outside the design space of the current fleet. If an ANOPP module is found to be unsuitable for the N2A or N2B, noise source data from an external model can be imported into ANOPP.

[1] Although EPNL is in decibels, FAR 36 uses a regular sum, rather than power 10 sum, for the cumulative EPNdB.

Table 3.1: Noise source estimation models for N2A and N2B noise assessment

Noise Source	Estimation Method
Fan, forward propagating	ANOPP Heidmann Fan Module *GE large turbofan method*
Fan, rearward propagating	ANOPP Heidmann Fan Module *GE large turbofan method*
Core	ANOPP GE Core Module
Jet (N2A)	ANOPP Stone 2 Jet Module
Jet (N2B)	Scaled SAX-40 jet noise hemisphere
Wing	FW-Hall physics-based airfoil self-noise method
Undercarriage	ANOPP Boeing Airframe Module *Modified landing gear model*
Elevon	ANOPP Boeing Airframe Module *Modeled as aileron*
Leading edge droop	Droop effect on BL properties included in FW-Hall Contributions from side edge not modeled
Wing tip (N2A) Winglet (N2B)	Tip vortex noise model by Brooks & Marcolini [29]
Vertical Tail (N2A)	ANOPP Fink Airframe Module

3.3 Overview of Noise Sources

For the N2A and the N2B, a combination of ANOPP modules and several external models were used to calculate their noise sources. The models are summarized in Table 3.1.

Engine noise estimation was provided by NASA GRC. ANOPP modules were used for engine noise with input from NASA's Numerical Propulsion System Simulation (NPSS) code. However, due to the triple-slotted configuration of the N2B exhaust nozzle, the ANOPP Stone 2 Jet Module cannot adequately model the N2B jet noise. Therefore, the jet noise hemisphere[2] from the SAX-40 was scaled up using the ratio of the SAX-40F jet Mach number to the SAX-40 jet Mach number. Based on dimensional analysis, the acoustic pressure is proportional to the 8^{th} power of jet Mach number [30].

ANOPP modules were used for most of the airframe noise sources. For wing noise,

[2]The noise hemisphere is sound pressure level measured on a 100-ft radius hemisphere on the right side of the aircraft.

Table 3.2: Noise attenuation estimation models for N2A and N2B noise assessment

Installation Effect	Estimation Method
Fan forward shielding	Ray tracing calculations on SAX-40 airframe
Fan rearward shielding (N2A)	ANOPP barrier shielding method
Core shielding (N2A)	ANOPP barrier shielding method
Jet shielding (N2A)	UCI jet shielding experimental data *Includes perforated wedge on nozzle*
Fan forward acoustic liner	ANOPP TREAT Module *GE large turbofan method*
Fan rearward acoustic liner	ANOPP TREAT Module *GE large turbofan method*
Landing gear fairing	SAX-40 landing gear fairing experimental data *Applied as decrement to undercarriage noise*

an airfoil self-noise method based on the the FW-Hall formulation was used. It was conceived during the Silent Aircraft Initiative by Manneville, Pilczer, and Spakovszky [31] and further developed by Hileman and Spakovszky. The noise amplitude due to the scattering of turbulent eddies at the trailing edge was calculated using Lighthill's acoustic analogy based on the work of Ffowcs-Williams and Hall [32], while the directivity and spectral shape were calculated from empirical correlations. The advantage is that the FW-Hall method is based on boundary layer properties derived from a viscous airfoil calculation, rather than broad correlations using global geometric parameters. Its results were found to agree well with ANOPP's Fink method.

3.4 Propulsion System Installation Effects

Similar to the noise sources, a combination of ANOPP modules and external models were used to estimate the attenuation of the noise sources due to installation effects of the propulsion system on the N2A podded engine aircraft and the N2B embedded engine aircraft. These are calculated separately from the noise source estimation and applied as an increment or decrement in ΔdB to the source sound pressure level (SPL). The models are summarized in Table 3.2.

An assessment of ANOPP's noise shielding prediction capability showed that its

current barrier shielding method is unsuitable for HWB aircraft configurations such as the N2A and the N2B. It was derived from the work of Beranek [15] and Maekawa [16] to estimate the effectiveness of noise barriers based on an empirical correlation of noise attenuation to Fresnel's number for a semi-infinite rectangular screen. Essentially, it calculates noise attenuation due to a straight edge and is therefore incompatible with the planform shape of the N2A and the N2B. Furthermore, it considers only a monopole source and cannot handle the distributed nature of the jet noise source. Based on these considerations, the applicability of the barrier shielding method in the N2A and N2B noise assessment was limited.

Thus, previously computed ray tracing results for the SAX-40 [1] were applied to the fan forward noise in the N2A and N2B noise assessment. Although ray tracing is a higher fidelity method, it is also much more complex and computationally expensive. Therefore, ray tracing was not computed directly on the N2A and N2B airframe. Instead, the SAX-40 ray tracing results were applied to the N2A with the caveat that the N2A has two engines instead of three and vertical tails instead of winglets. For the N2B, the geometry is similar to the SAX-40 geometry such that the SAX-40 ray tracing results were expected yield reasonable results.

ANOPP's barrier shielding method was applied to estimate the rearward propagating turbomachinery noise, i.e. fan rearward and core, of the N2A configuration[3]. This is because shielding is provided by the aircraft trailing edge, which can be reasonably approximated as a straight edge. For the distributed N2A jet noise source, UCI performed experimental measurements of trailing edge shielding attenuation that was applied to the noise assessment. A perforated wedge was inserted into the top part of the nozzle annulus to compact the distributed noise source and increase shielding effectiveness.

It was clear that in order to perform a more rigorous noise assessment of the N2A and the N2B and to evaluate the benefits of other noise reduction techniques, an improved noise shielding prediction method is required. To this end, a diffraction integral method for turbomachinery noise shielding prediction was implemented and

[3]The N2B engine nozzles extend beyond the trailing edge and are unshielded.

is described in Chapter 4. At the same time, UCI is developing a jet noise shielding method based on their experimental findings.

3.5 N+2 Noise Audit Results

Combination of all noise sources and effects in ANOPP over the FAR 36 compliant LTO trajectories revealed that the N2A was close to meeting the N+2 noise goal. The results of the noise assessment are presented in Sections 3.5.1 and 3.5.2 as time histories of tone-corrected perceived noise level (PNLT) for each of the approach, lateral, and flyover conditions. The PNLT plots were broken down into each of the noise sources, including separate entries for the nose and main landing gears. The N2A elevons were also divided into inboard elevons and outboard elevons relative to the location of the vertical tail. The PNLT data were then integrated to obtain the EPNL for comparison to NASA's N+2 noise goal.

3.5.1 N2A Tone-Corrected Perceived Noise Levels

The N2A approach, lateral, and flyover noise are shown in Figures 3-1, 3-2, and 3-3, respectively. The times at which the aircraft is directly above the observer (or to the side, in the case of the lateral noise monitor) are also indicated on the plots. The drop in engine noise at about 91 seconds during flyover is due to thrust cutback, while the jump in fan rearward and core noise at about 71 seconds during lateral and 117 seconds during flyover are due to the observer moving out of the shadow zone of the trailing edge. Due to its distributed nature, the jet noise source did not exhibit the same sharp jump.

The noise assessment of the N2A aircraft indicates that jet noise and fan rearward noise need further reduction. The two noise sources are the dominant contribution to the total noise at both take-off monitor locations, i.e. lateral and flyover. However, the margin for improvement in flyover is much lower unless elevon noise is also reduced along with the jet noise and the fan rearward noise. On approach, the airframe noise sources are more significant due to the low engine power setting. The loudest approach

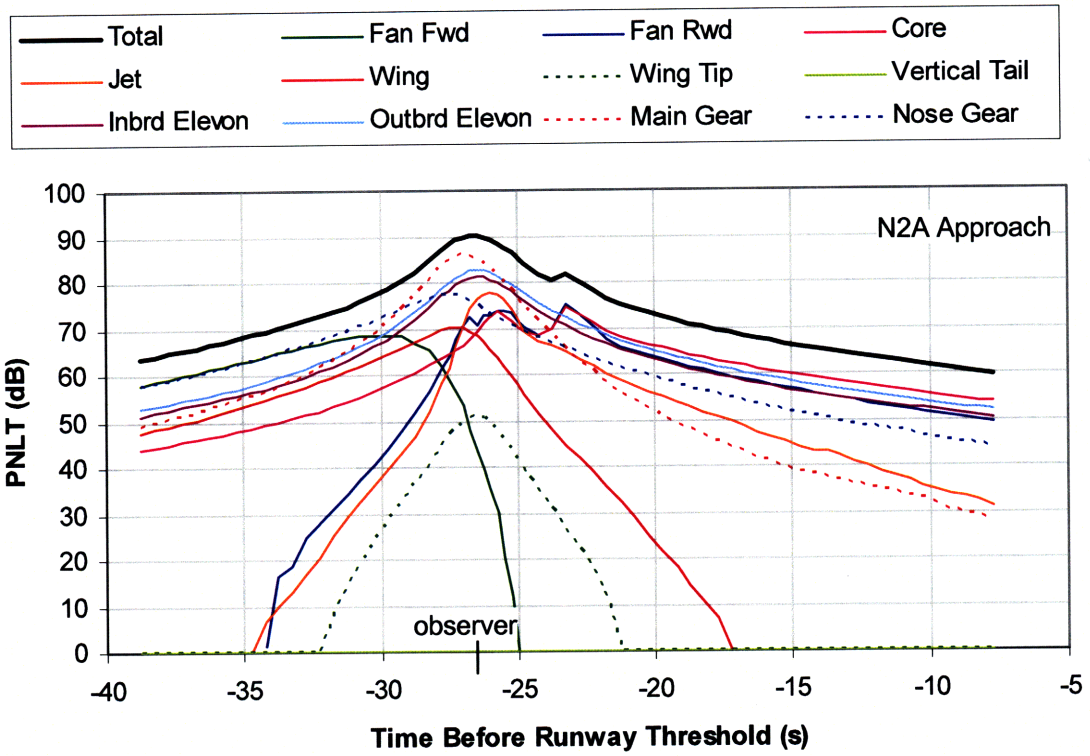

Figure 3-1: Tone-corrected perceived noise level for the N2A on approach

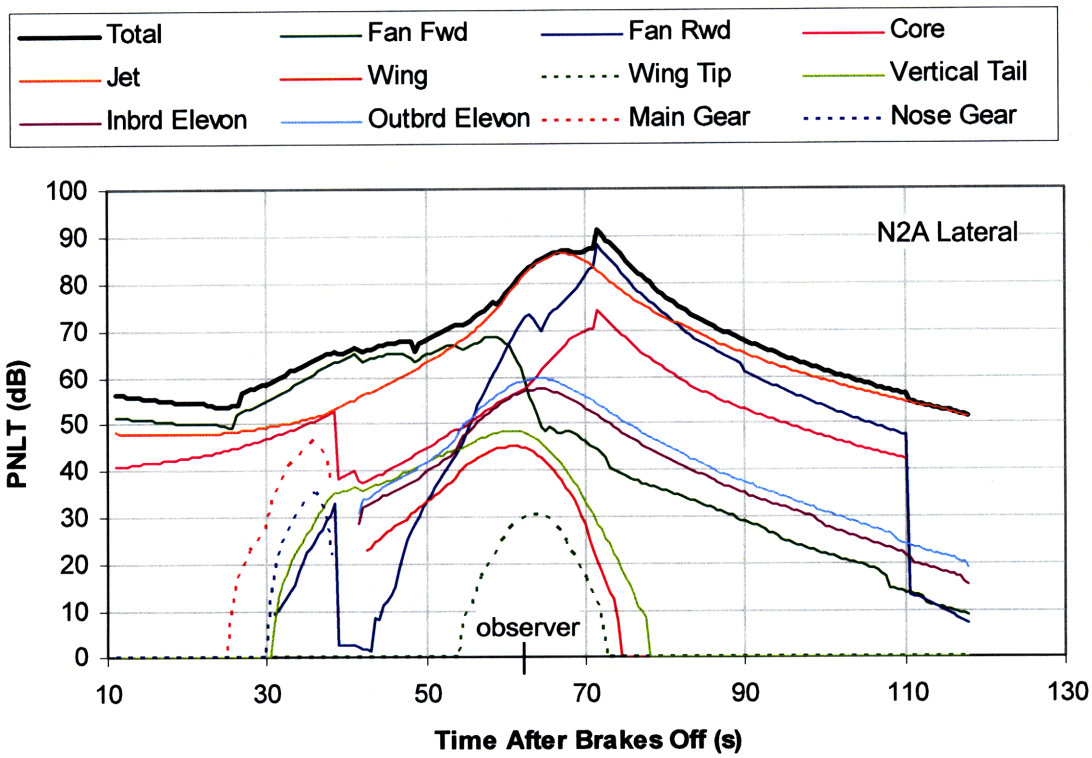

Figure 3-2: Tone-corrected perceived noise level for the N2A at lateral

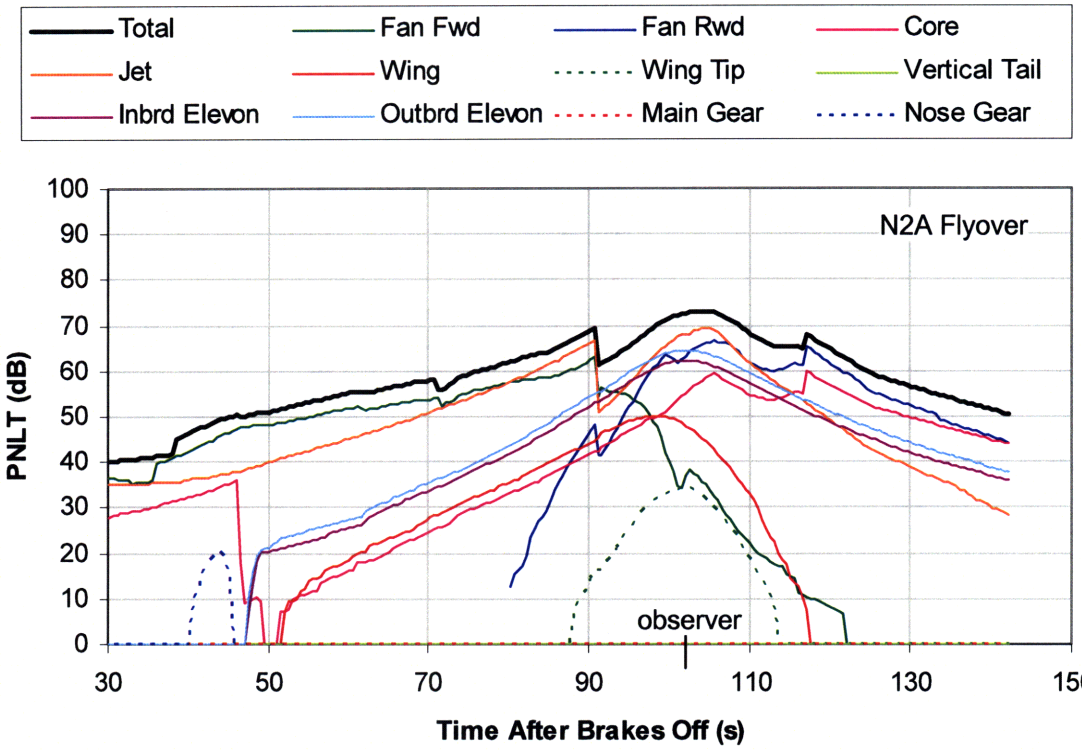

Figure 3-3: Tone-corrected perceived noise level for the N2A at flyover

noise source is the main landing gear, followed by the elevons.

3.5.2 N2B Tone-Corrected Perceived Noise Levels

The N2B approach, lateral, and flyover noise are shown in Figures 3-4, 3-5, and 3-6, respectively. The times at which the aircraft is directly above the observer (or to the side, in the case of the lateral noise monitor) are also indicated on the plots. Like the N2A, the drop in engine noise at about 91 seconds during flyover is due to thrust cutback. However, unlike the N2A, there is no jump in fan rearward or core noise due to the lack of engine exhaust shielding.

Due to the complexity of the embedded propulsion system and the lack of ANOPP's capability to model such a propulsion system, the N2B engine noise, while dominant in all three cases, may not be representative of the actual noise level. Current ANOPP modules were not developed to model the N2B engine configuration of three fans powered by a single core. Furthermore, the ANOPP TREAT acoustic liner module was limited by the length of acoustic liners it could model and was not able to estimate

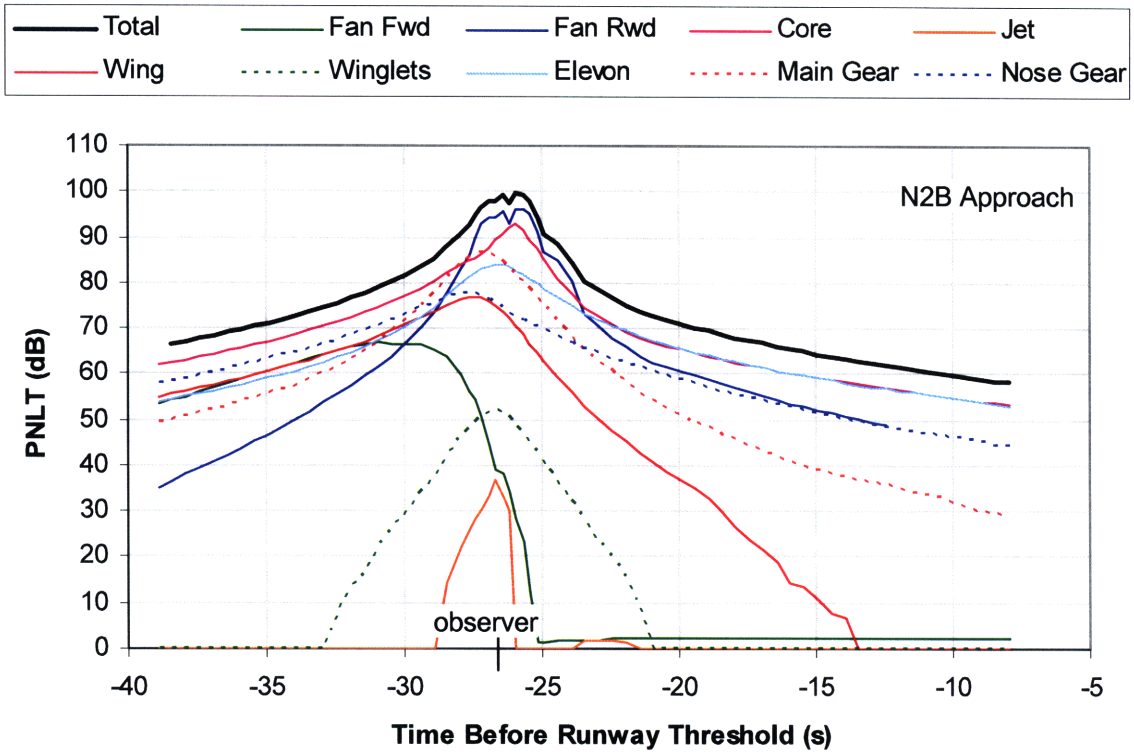

Figure 3-4: Tone-corrected perceived noise level for the N2B on approach

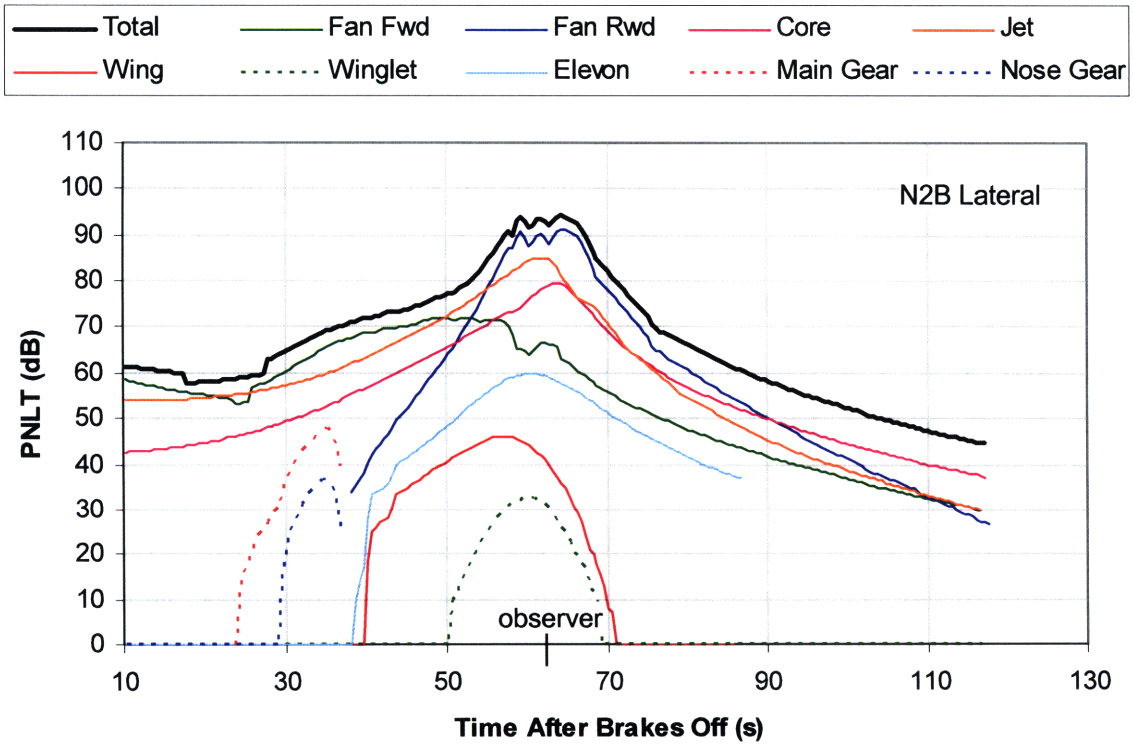

Figure 3-5: Tone-corrected perceived noise level for the N2B at lateral

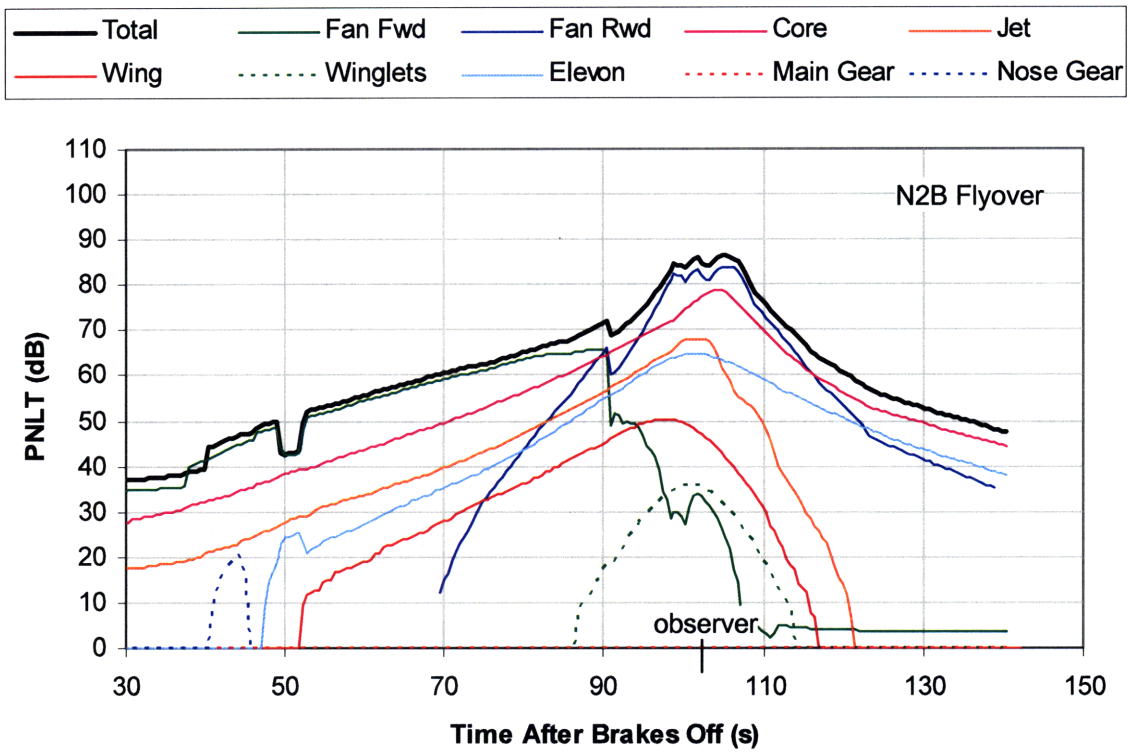

Figure 3-6: Tone-corrected perceived noise level for the N2B at flyover

the noise attenuation for the full length of the acoustic liners in the N2B engines. This, in combination with the lack of shielding for the engine exhaust, resulted in the significant overestimation of the engine noise compared to the Silent Aircraft Initiative. Unfortunately, the SAX-40 engine noise was estimated using Rolls-Royce's proprietary codes and is not available for the N+2 project. Therefore, until advanced ANOPP engine noise prediction methods are in place, the N2B noise results should be considered preliminary.

An exception to the otherwise overestimated N2B engine noise is the jet noise. It is suspected that the low power setting on approach made it inappropriate to scale the SAX-40 jet noise hemisphere, resulting in unreasonably low jet noise. Overall, refinement and improvement in engine noise modeling is recommended before further analysis into the N2B noise results. This is the focus of current and future work under the NASA N+2 program.

Table 3.3: Effective perceived noise and FAR 36 Stage 3 noise limits [2]

	N2A	Stage 3	N2B	Stage 3
Approach	86.8	102.7	93.6	102.7
Lateral	90.1	100.4	94.1	100.4
Flyover	76.9	97.0	87.0	100.0
Cumulative	253.8	300.1	274.7	303.1
Difference from N+2 Goal	-5.7		-23.6	

3.5.3 Comparison of Effective Perceived Noise Level to N+2 Goal

Table 3.3 shows that the N+2 noise goal of -52 EPNdB relative to Stage 3 was not yet achieved. The N2A is 5.7 EPNdB short of the noise goal but further low-noise improvements to the aircraft are expected to bring the N2A to the goal. The N2B is 23.6 EPNdB short of the noise goal but, as mentioned previously, adequate noise estimation methods for the N2B engines are not yet in place. Thus, the reliability of the N2B EPNL is uncertain.

In order to meet the N+2 noise goal, the following modifications to the N2A and N2B are suggested:

- Redesign the engine cycle at a lower fan pressure ratio to reduce jet noise and fan noise.
- Employ more acoustic liners along the N2B engine ducts.
- Further develop advanced low-noise landing gear fairings.
- Mitigate elevon side edge noise with continuous mold-line or other techniques.

The above suggestions were made based on the breakdown of PNLT for each noise source in Sections 3.5.1 and 3.5.2. In particular, the engine cycle redesign for low noise takes advantage of the gap between the fan and jet noise and the next loudest noise source in the lateral monitor case, as shown in Figure 3-2. Figure 3-1 shows that advanced landing gear fairings can be used to lower the peak main gear noise on

approach by about 3 dB. Further noise reduction will require concurrent mitigation of elevon side edge noise.

To evaluate the suggested modifications and to increase the fidelity of the noise assessment, the following improvements to the noise estimation methods are recommended:

- Develop engine noise estimation methods for the N2B engine configuration.
- Increase the fidelity of turbomachinery noise shielding prediction for the HWB planform geometry.
- Develop a jet noise shielding prediction method that accounts for the distributed nature of the jet noise source.
- Increase the fidelity of the acoustic liner model.

Advanced method development for unconventional aircraft is one of the main objectives of the N+2 project. Turbomachinary noise shielding was part of MIT's responsibility and is the subject of the next chapter.

Chapter 4

Acoustic Shielding Prediction

A diffraction integral method for turbomachinery noise shielding prediction was implemented as an improved alternative to the barrier shielding method currently used in ANOPP. It is based on Maggi and Rubinowicz's formulation of the Kirchhoff diffraction theory and was first used for aircraft noise shielding by Lummer [17]. A key advantage of the diffraction integral method over the barrier shielding method is that it is applicable to object geometries more general than a semi-infinite rectangular screen. This is particularly important for an HWB type airframe because of its unconventional planform shape. Therefore, the goal is to improve ANOPP's turbomachinery noise shielding module and to predict N2A and N2B shielding based on this formulation. The derivation and implementation of the diffraction integral method are described in this chapter.

4.1 Comparison of Shielding Prediction Methods

The rationale for implementing the diffraction integral method follows the comparison of current methods used for noise shielding prediction and the examination of past work in the noise shielding prediction of the HWB aircraft configuration.

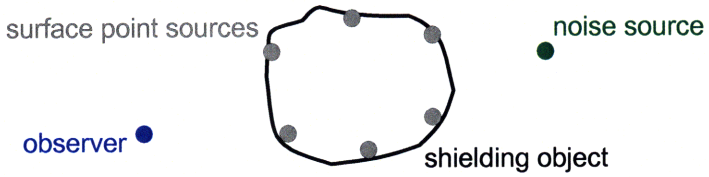

Figure 4-1: Schematic of the fictitious point sources on the object surface in the boundary element method

4.1.1 Boundary Element Method

The boundary element method (BEM) represents acoustic pressure at the observer as a sum of the contributions from fictitious point sources distributed on the surface of the shielding object. This is illustrated in Figure 4-1. The algorithm then solves for the strengths of surface point sources that satisfy the boundary condition. This is essentially a numerical implementation of Green's theorem integral equation for acoustic scattering. A limitation of this method is that the discretization of the shielding object must be fine enough to resolve the wavelength of the noise source. As a result, the number of grid points scale with the surface area and the square of the wave number. Thus, the method becomes computationally impractical for large objects at high frequencies.

During the Silent Aircraft Initiative, Agarwal and Dowling [14] applied the boundary element method to estimate the noise shielding effectiveness the SAX-40 HWB airframe. They found that Taylor's transformation can be used to decouple the flow equation and the wave equation, allowing the BEM to predict shielding of an airframe in a low Mach number potential flow. However, due to the BEM frequency limitation, the SAX-40 shielding was calculated at $ka = 50$, where k is the wave number and a is the center body chord, or about 50 Hz. Agarwal and Dowling extended the solution in an approximate manner to higher frequencies using the inverse square-root dependence of acoustic pressure to frequency. They found about 18 dB reduction in OASPL due to noise shielding, indicating significant low-noise benefit of the HWB configuration.

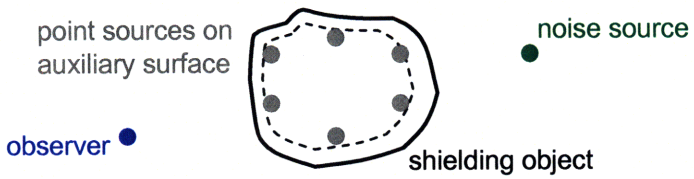

Figure 4-2: Schematic of the point sources on a smaller auxiliary surface in the equivalent source method

4.1.2 Equivalent Source Method

The equivalent source method makes it possible to run at higher frequencies relative to the typical boundary element formulation by locating the fictitious point sources on an auxiliary surface within the shielding object, as illustrated in Figure 4-2. An example of the equivalent source method is NASA's Fast Scattering Code (FSC) [33], which places the point sources on a 90% scaled replica of the shielding object. This reduces the number of grid points required by 2/3 relative to typical boundary element methods. Although the Fast Scattering Code is able to solve higher frequency shielding problems, the number of grid points required is still limited by the same scaling rule as the boundary element method, i.e. $N \propto k^2 A$, where N is the number of grid points, k is the wave number, and A is the surface area of the shielding object.

The Fast Scattering Code was applied to the blended-wing-body aircraft configuration by Reimann, Tinetti, and Dunn [34]. They were able predict the sound pressure level of source and nacelle combinations and found reasonable agreement with experimental measurements. However, computational time limited the predictions to less than 315 Hz. Experiments of the source and nacelle combination shielded by the blended-wing-body airframe found that the amount of shielding, while negligible at low frequencies, increases with frequencies. This suggests that it is important to be able to directly calculate noise shielding at high frequencies of up to 10,000 Hz, the highest of the 24 center frequencies of the $\frac{1}{3}$-octave band. At such high frequencies, both the boundary element method and the equivalent source method are impractical and an alternate method based on ray theory can be used.

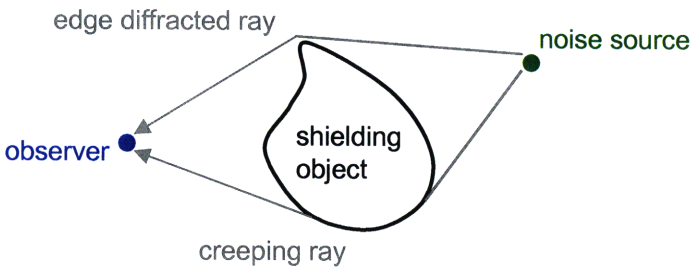

Figure 4-3: Schematic of the two types of rays in the ray tracing method: edge diffracted rays and creeping rays

4.1.3 Ray Tracing Method

The ray tracing method is a high frequency method that is accurate when the wavelength is much shorter than the dimensions of the shielding object. Asymptotic expansion of the wave equation for $ka \gg 1$, where k is the wave number and a is the characteristic length of the shielding object, results in geometric acoustics where sound propagates as acoustic rays. Furthermore, the acoustic rays are straight lines in low Mach number potential flow [1]. For observers in the acoustic shadow behind a shielding object, the geometric theory of diffraction allows rays that strike the object to reach the shadow region as edge diffracted rays or creeping rays. An edge diffracted ray occurs when the incident ray strikes a sharp edge on the object, while a creeping ray occurs when the incident ray is tangent to the object and creeps along a smooth surface. The two types of diffracted rays are illustrated in Figure 4-3.

Van Rens et al. [35] demonstrated the ray tracing method by calculating the creeping rays around a blended-wing-body aircraft. During the Silent Aircraft Initiative, Agarwal et al. [1] further developed the ray tracing method by incorporating both creeping rays and edge diffracted rays. One advantage of the method is that it provides a way to relate the shielding level to the object shape. Agarwal et al. showed that the leading edge of winglets diffract multiple rays toward observers below and behind the winglets. Summing these multiple rays resulted in reduced shielding at those observer locations. This insight may be used to improve the shielding effectiveness of the airframe.

While the ray tracing method is applicable to high frequency shielding problems

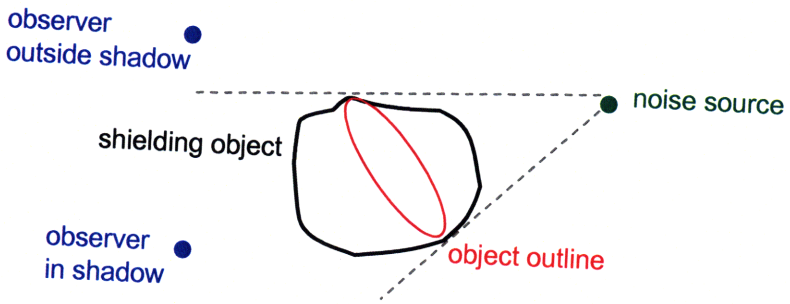

Figure 4-4: Schematic of the object outline for the contour of integration in the diffraction integral method

such as engine noise shielded by a large airframe, the geometric theory of diffraction is very complex and challenging to implement. Furthermore, the computational cost to calculate creeping rays can be expensive. As a result, it is not an attractive method for ANOPP. Instead, a simplified version of ray tracing, called the diffraction integral method, provides a faster and simpler alternative.

4.1.4 Diffraction Integral Method

The diffraction integral method replaces the geometric theory of diffraction with a contour integral, where the contour of integration is the outermost outline on the object dividing the illuminated side and the shadow side. A schematic is shown in Figure 4-4. The advantages of this approach include:

- Applicable to more complex geometries than barrier shielding method.
- Based on first principles, not empirical correlations.
- Relatively fast computational time requiring only a 1-D numerical integration.
- Accurate at high frequencies that are difficult to compute with BEM.
- Does not require full 3-D object geometry, as long as the outline can be estimated.

For these reasons, the diffraction integral method was proposed to replace ANOPP's barrier shielding method. However, it is not expected to replace the boundary element

method, the equivalent source method, or the ray tracing method when high fidelity is required. Unlike the ray tracing method, which is exact as $ka \to \infty$, the diffraction integral method is an approximation. However, the approximation becomes better at higher frequencies. The assumption used in the derivation of the method is explained below.

4.2 Derivation of the Diffraction Integral Method

The diffraction integral method is based on the Kirchhoff diffraction integral, which is an approximation to the Green's theorem solution of the Helmholtz equation. This integral can be solved analytically to calculate diffraction for simple shielding geometries. The idea here is to evaluate the integral numerically for more complex geometries. Three main steps need to be taken to derive the desired form of the diffraction integral:

1. Apply the Green's theorem integral equation to a screen with an aperture, where the boundary conditions can be approximated.

2. Transform the surface integral into a contour integral based on Stoke's theorem.

3. Obtain the diffraction around a shielding object by calculating the complementary solution to the diffraction through an aperture.

The noise attenuation due to shielding can then be calculated from the ratio of the total acoustic pressure (incident + diffracted) to the incident acoustic pressure without any diffraction:

$$\Delta SPL = 20 \log \left| \frac{p_i + p_d}{p_i} \right| \tag{4.1}$$

where ΔSPL is the change in sound pressure level (SPL) due to shielding in ΔdB, p_i is the incident acoustic pressure without diffraction, and p_d is the acoustic pressure diffracted by the shielding object.

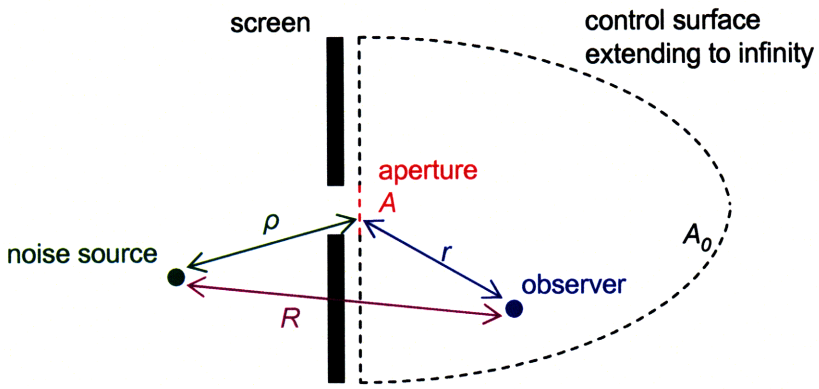

Figure 4-5: Control surface for Green's theorem behind the screen with an aperture

4.2.1 Kirchhoff Diffraction Integral

The Kirchhoff diffraction integral is a simplification of the Green's theorem solution to the Helmholtz equation for the special case of diffraction through an aperture in a screen. The setup is illustrated in Figure 4-5.

The incident acoustic pressure for a monopole noise source and the diffracted acoustic pressure from the Green's theorem integral equation are

$$p_i(\vec{r}) = \frac{e^{ikR}}{R} \tag{4.2}$$

$$p_d(\vec{r}) = \frac{1}{4\pi} \oiint_{A+A_0} \left[\frac{e^{ikr}}{r} \frac{\partial p_d}{\partial n} + p_d \frac{\partial}{\partial n} \left(\frac{e^{ikr}}{r} \right) \right] \mathrm{d}S \tag{4.3}$$

Equation 4.3 is an integral equation where p_d on the surface is unknown. BEM turns the surface integral into a system of equations by approximating the boundary values of p_d as point sources of unknown strength. Here, the boundary values of p_d are approximated for the screen with an aperture so that the integral can be evaluated explicitly. Referring to Figure 4-5, an assumption is made that the pressure behind the screen is zero and the pressure at the aperture is equal to the incident pressure from the noise source. Furthermore, the screen is rigid so that the normal derivative of pressure on the screen is also zero. This assumption is justified at high frequencies where geometric acoustics apply. The remainder of the control surface extends to infinity so that the pressure and its normal derivative vanish. Substituting the boundary conditions for p_d into Equation 4.3 results in the Kirchhoff diffraction

integral

$$p_{d,A}(\vec{r}) = \frac{1}{4\pi} \iint_A \left[\frac{e^{ikr}}{r} \frac{\partial}{\partial n} \left(\frac{e^{ik\rho}}{\rho} \right) + \frac{e^{ik\rho}}{\rho} \frac{\partial}{\partial n} \left(\frac{e^{ikr}}{r} \right) \right] \mathrm{d}S \tag{4.4}$$

The integral is now in terms of known geometric parameters and is integrated over the area of the aperture only.

4.2.2 Maggi-Rubinowicz Transformation

To reduce the computational time for the numerical integration, the Kirchhoff diffraction integral is transformed from a surface integral into a contour integral. The control surface in Figure 4-5 is arbitrary as long as it follows the back side of the screen. Therefore, the surface A in the Kirchhoff diffraction integral, Equation 4.4, is arbitrary as long as it is bounded by the rim of the aperture on the screen. It then follows that the surface integral can be transformed into a contour integral, where the contour of integration, ∂A, is the rim of the aperture. This transformation for the Kirchhoff diffraction integral was derived independently by Maggi and Rubinowicz and is detailed in Sommerfeld [36]. The result is

$$p_{d,A}(\vec{r}) = \frac{1}{4\pi} \oint_{\partial A} \frac{e^{ik\rho}}{\rho} \frac{e^{ikr}}{r} \frac{(\vec{\rho} \times \vec{r}) \cdot \mathrm{d}\vec{s}}{\rho r + \vec{\rho} \cdot \vec{r}} + \chi \frac{e^{ikR}}{R} \tag{4.5}$$

$$\chi = \begin{cases} 1 & \text{if } \vec{R} \text{ goes through } \partial A \\ 0 & \text{otherwise} \end{cases}$$

Note that while the Kirchhoff diffraction integral may be derived for point sources with non-uniform directivity, the Maggi-Rubinowicz transformation assumes a monopole source.

4.2.3 Babinet's Principle

Babinet's principle provides a way to interchange the aperture and the screen, effectively turning the diffraction through an aperture into the diffraction around a shielding object. It is a property of the Kirchhoff diffaction integral which states that the sum of diffracted pressures due to complementary screens is equal to the

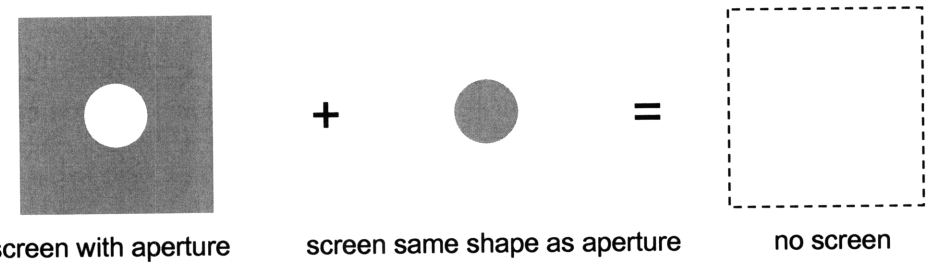

Figure 4-6: Illustration of Babinet's principle for complementary screens

undiffracted free-field pressure. This is illustrated schematically in Figure 4-6.

A screen that is complementary to the shielding object, such as the HWB airframe, is one in which the rim of its aperture divides the illuminated side and the shadow side of the object. This aperture rim can also be interpreted as the outermost outline of the shielding object from the point of view of the noise source and is the contour of integration for Equation 4.5.

Combining all the pieces, the first part of the diffraction integral method is to determine the outline of the shielding object based on the source location. Next, the contour integral is solved numerically to obtain the diffracted pressure through an aperture with the shape of the outline, $p_{d,A}$. Finally, the diffracted pressure for the shielding object, $p_{d,O}$ is obtained by subtracting $p_{d,A}$ from the free-field, i.e.

$$p_{d,O} = p_i - p_{d,A} \tag{4.6}$$

The noise attenuation due to shielding can then be obtained from Equation 4.1.

4.3 Implementation of the Diffraction Integral Method

The implementation of the diffraction integral method for integration with ANOPP is divided into two parts: the "offline part" and the "online part". A flowchart is shown in Figure 4-7.

The offline part determines the object outline for the contour of integration. This

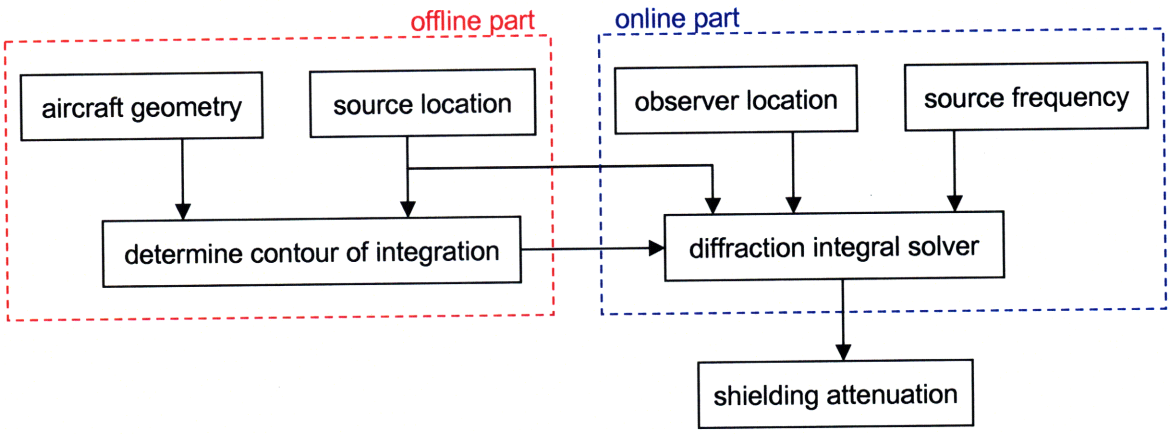

Figure 4-7: Two-part implementation of the diffraction integral method

can be a separate calculation from the ANOPP noise estimation and is run only once for each aircraft geometry. If the object outline can be estimated, e.g. using leading edge and trailing edge coordinates of the aircraft planform, then the offline part is not needed.

The online part evaluates the diffraction integral to obtain the noise attenuation due to shielding for each observer location and each frequency. This would take the place of ANOPP's Wing module, which employs the barrier shielding method, and is run as part of ANOPP's noise estimation.

Both parts have been coded in Matlab® to demonstrate and validate the algorithm, which is explained in detail in Sections 4.3.1 and 4.3.2.

4.3.1 Determination of Shielding Object Outline

The main challenge to determine the outline of the shielding object is to find the coordinates of the points on the object surface and then connect them into a single, closed contour. The algorithm involves the following steps:

- Find contours comprised of points on the object surface that are tangent to the rays from the source.
- Project contours onto a sphere centered around the source.
- Rasterize the projected contours to extract the outermost outline.

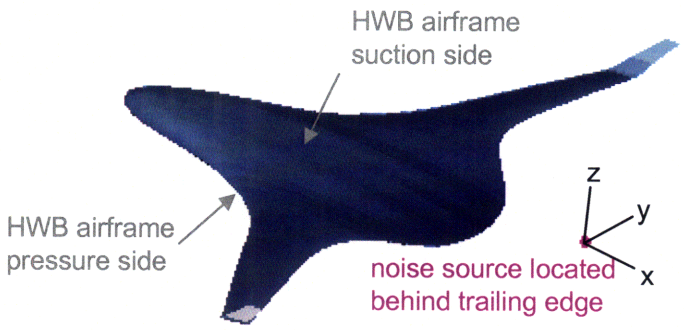

Figure 4-8: A hypothetical HWB aircraft with the engine noise source located behind the trailing edge

- Return the projected outermost outline back to 3-D coordinates.

The steps are explained in more detail below. A hypothetical HWB aircraft with the noise source located behind the trailing edge, as shown in Figure 4-8, is used illustrate the procedure. The coordinate system relative to the aircraft is defined as follows: x = aft, y = starboard, and z = up. Although this is an unsual configuration for shielding (shielding will be seen by observers directly in front of the aircraft, not below the aircraft), this geometry was chosen because it highlights challenges that are not present for a noise source located above the airframe. It demonstrates the robustness of the algorithm in handling situations where the noise source sees both the suction surface and the pressure surface of the aircraft.

Step 1: Find Tangent Contours

The object surface is discretized into quadrilateral panels whose vertices are coordinates from the geometry input. There are two outward normals associated with every edge, corresponding to its two adjacent panels. Dot products are calculated between the ray from the source to the edge and the two normals associated with that edge. If the two dot products are opposite in sign, that edge is selected because it forms part of the object surface that is tangent to the rays from the source. The endpoints of all selected edges are then strung together to form closed "tangent contours". This may result in several tangent contours. For example, the noise source of the hypothetical HWB sees a portion of both the suction surface and pressure surface of the airframe, as shown in Figure 4-9, resulting in tangent contours on both surfaces.

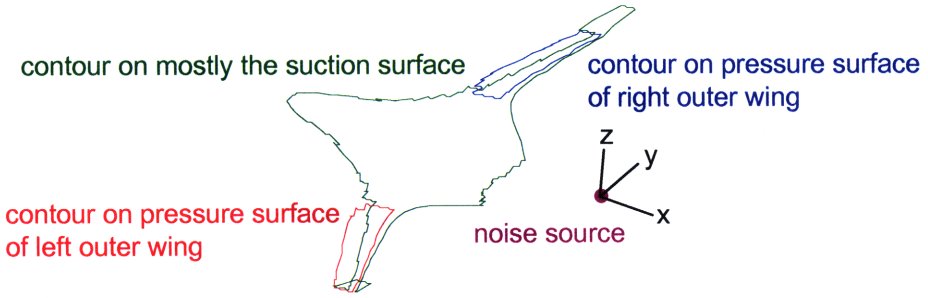

Figure 4-9: Contours tangent to the rays from the noise source for the hypothetical HWB

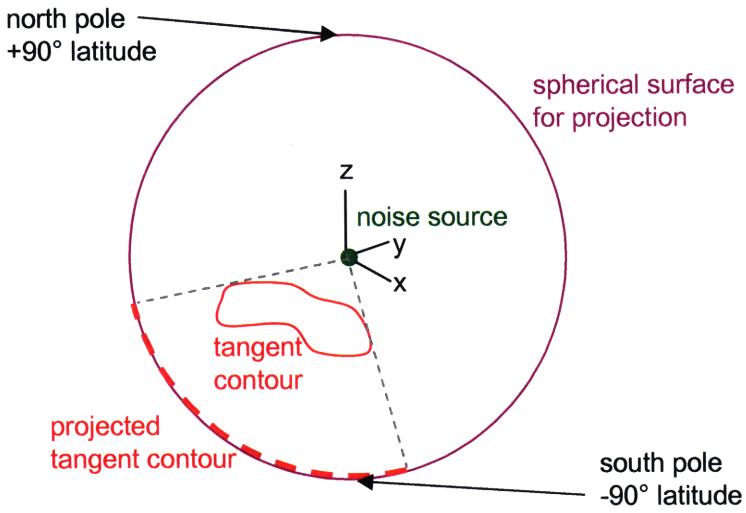

Figure 4-10: Illustration of the projection of a tangent contour onto a spherical surface centered around the source

Step 2: Project Contours

In order to represent the line-of-sight from the perspective of the noise source, the coordinates of the tangent contours are projected along rays from the source onto the surface of a sphere centered around the source. This is illustrated schematically in Figure 4-10. A sphere is chosen for the projection because a regular grid can be defined easily based on longitudes and latitudes. However, if a projected contour crosses the $\pm 180^\circ$ longitude, it must be divided into two separate contours. This is demonstrated by Figure 4-11, which shows half of the projected contours in the negative longitudes. A mirror image of Figure 4-11 exists in the positive longitudes.

Furthermore, if a projected contour encloses either the north pole or the south pole, it is divided along the $\pm 180^\circ$ longitude and closed along -90° latitude. It is

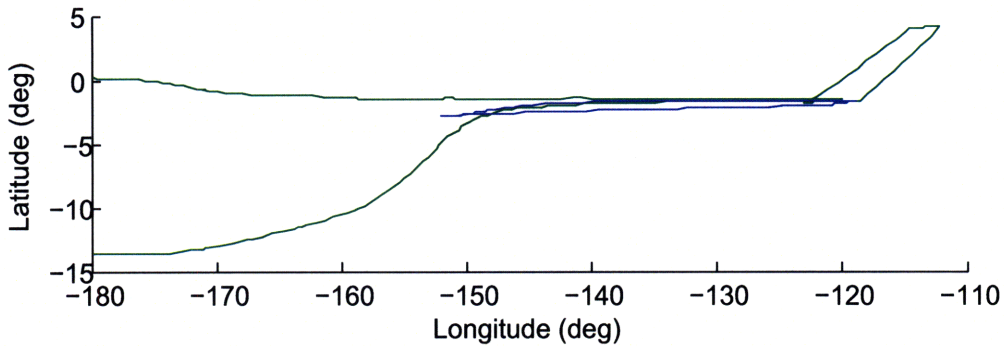

Figure 4-11: Projected contours of the hypothetical HWB in the longitude-latitude space

assumed that in this situation, the object obstructs the source line-of-sight in the negative z-direction and is clear of the positive z-direction. This is based on the usual case of observers located below the shielding object and the source located above the shielding object. If necessary, the coordinate system of the geometry can be redefined such that the source line-of-sight in the positive z-direction of the new coordinate system is not obstructed by any part of the object.

Step 3: Find Outermost Outline

A grid of evenly-spaced latitudes and longitudes is overlaid on top of the projected contours. All grid points that are enclosed by the projected contours are flagged. The outermost outline of the object can then be extracted by tracing the boundary between the flagged grid points and the unflagged grid points. Figure 4-12 shows the outline grid points of the hypothetical HWB in red. Comparing it with Figure 4-11 shows that the red outline is the outermost outline of all the projected contours.

Note that the grid must be fine enough to resolve the features of the projected contours. In particular, there must be enough grid points to distinguish between the inside, the boundary, and the outside of all portions of the projected contours.

Step 4: Return to 3-D Coordinates

To return the outermost outline of the shielding object from the 2-D longitude-latitude space back to 3-D coordinates, the segments of the projected tangent contours that

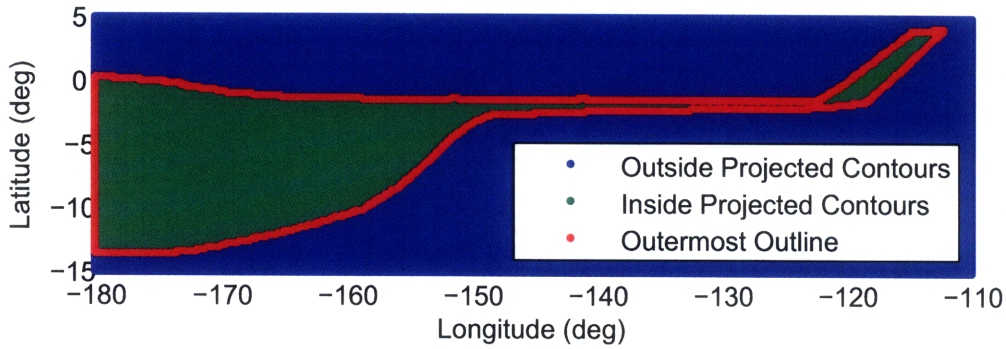

Figure 4-12: Grid points in the longitude-latitude space for the hypothetical HWB

correspond to the grid points selected as the outline are found. Using the longitude, latitude, and radius of the segments of the projected contours, the x, y, and z coordinates of the outline can then be calculated. However, a fine grid used in step 3 may result in too many points on the outline, which increases computational time during the numerical integration of the diffraction integral. Therefore, the points between two adjacent outline segments whose directions change by less than a specified angle are removed, eliminating redundant points that are almost colinear. This completes the procedure to determine the object outline for the contour of integration of the diffraction integral.

The final outline for the hypothetical HWB is shown in Figure 4-13. The outline is not smooth due to the coarseness and high aspect ratio of the panels used to define the airframe surface. Defining the airframe with more cross-sections and using less points per cross-section (i.e. to reduce the aspect ratio of surface panels) is expected to smooth the outline.

The input to the algorithm are the noise source coordinates and the object coordinates. The object coordinates are entered as a stack of planar cross-sections oriented in any of the xy, xz, or yz planes to accommodate geometries such as vertical tails, the wings, and fuselages, respectively[1]. Complex objects can be input as multiple components. The tangent contours for all components are projected onto the same sphere in step 2 to find the outermost outline for the entire object.

[1]Based on conventional aircraft coordinate system, where x is fuselage axis, y is span, and z is vertical.

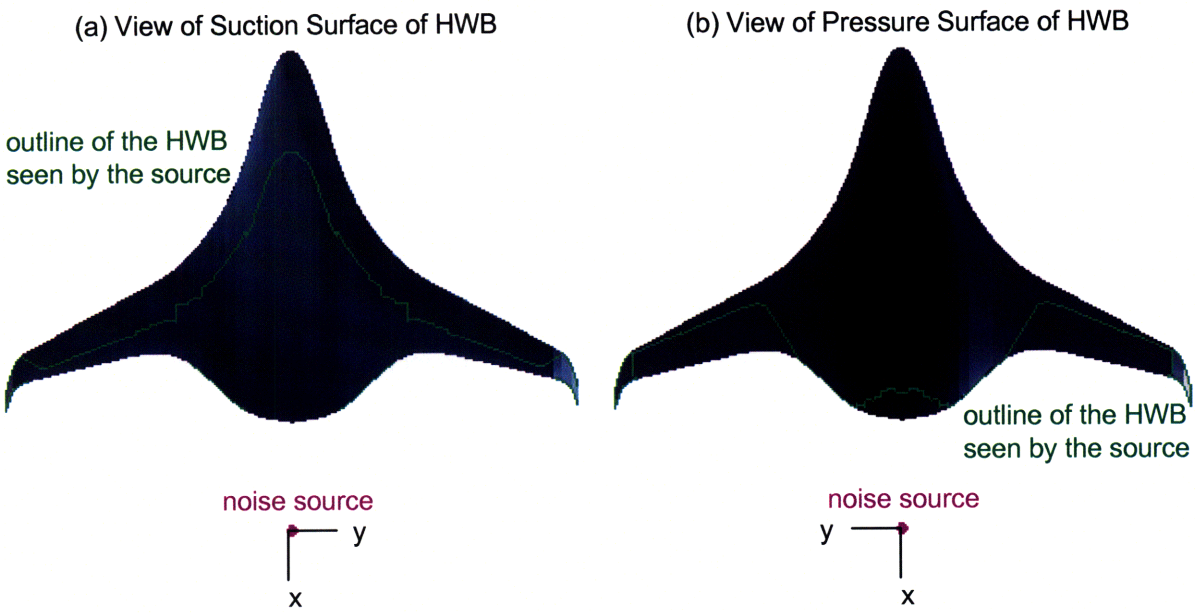

Figure 4-13: Final shielding outline for the hypothetical HWB

4.3.2 Contour Integral Evaluation

The two key challenges to evaluate the contour integral are checking if an observer lies inside the shadow region and handling the singularity of the integrand.

Observer in Shadow Region

The χ factor in the contour integral, Equation 4.5, is 1 if the observer lies in the shadow region and 0 otherwise. To determine the value of χ, the object outline and the observer locations are projected onto the surface of a circular paraboloid that opens upward in the positive z-direction, as illustrated in Figure 4-14. The projected outline can then be treated as a polygon by considering the x and y coordinates of the projection. A standard algorithm for "inside polygon check" is employed to determine if the projected observers lie within the projected outline. If true, $\chi = 1$; otherwise $\chi = 0$. A paraboloid is used here for the projection because unlike in Section 4.3.1, a regular grid is not required and the paraboloid avoids the problem of crossing the $\pm 180\,^{\circ}$ longitude.

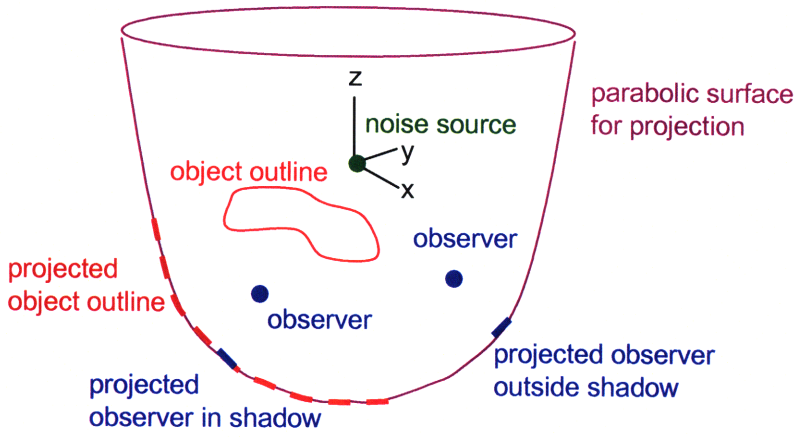

Figure 4-14: Illustration of the projection of the object outline and observer points onto a circular paraboloid

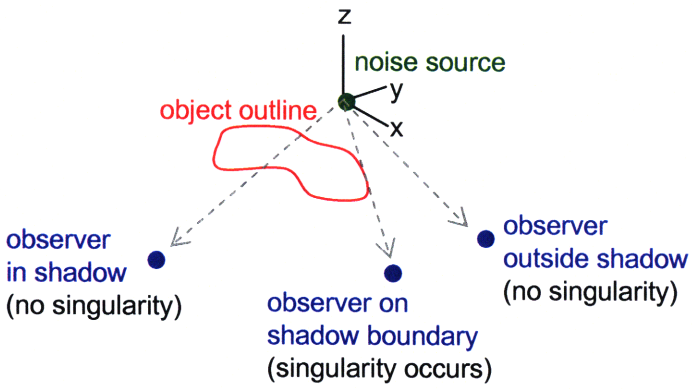

Figure 4-15: Illustration of when the integrand singularity occurs and when it does not occur

Integrand Singularity

Defining the noise source coordinates as $\vec{z}$, observer coordinates as $\vec{x}$, and a point on the contour of integration as $\vec{y}(s)$, where s is the distance along the contour, then the vectors $\vec{\rho}(s) = \vec{y}(s) - \vec{z}$ and $\vec{r}(s) = \vec{y}(s) - \vec{x}$. The integrand in the diffraction integral, Equation 4.5, becomes singular when $\rho r + \vec{\rho} \cdot \vec{r} = 0$. This occurs when the points $\vec{z}$, $\vec{x}$, and $\vec{y}(s)$ are colinear, i.e. the line-of-sight from the source to the observer touches the contour of integration, rather than going inside or outside of it. This is illustrated schematically in Figure 4-15. In order to evaluate the integral, Lummer [17] found that the singular part of the integrand can be subtracted out and then integrated analytically for a straight line segment. His derivations are described below.

The diffraction integral can be separated as follows:

$$\begin{aligned} p_{d,A}(\vec{r}) &= \frac{1}{4\pi}\oint_{\partial A}\frac{e^{ik\rho}}{\rho}\frac{e^{ikr}}{r}\frac{(\vec{\rho}\times\vec{r})\cdot \mathrm{d}\vec{s}}{\rho r+\vec{\rho}\cdot\vec{r}}+\chi\frac{e^{ikR}}{R} \\ &= \frac{1}{4\pi}\oint_{\partial A} e^{ik(\rho+r)}\left(1-\frac{\vec{\rho}\cdot\vec{r}}{\rho r}\right)\frac{(\vec{\rho}\times\vec{r})\cdot \mathrm{d}\vec{s}}{(\vec{\rho}\times\vec{r})^2}+\chi\frac{e^{ikR}}{R} \\ &= I_1+I_2+\chi\frac{e^{ikR}}{R} \end{aligned} \tag{4.7}$$

where

$$I_1 = \frac{e^{ikR}}{4\pi}\oint_{\partial A}\left[e^{ik(\rho+r-R)}\left(1-\frac{\vec{\rho}\cdot\vec{r}}{\rho r}\right)-2\right]\frac{(\vec{\rho}\times\vec{r})\cdot \mathrm{d}\vec{s}}{(\vec{\rho}\times\vec{r})^2} \tag{4.8}$$

$$I_2 = \frac{e^{ikR}}{4\pi}\oint_{\partial A}\frac{2(\vec{\rho}\times\vec{r})\cdot \mathrm{d}\vec{s}}{(\vec{\rho}\times\vec{r})^2} \tag{4.9}$$

The singularity is contained in I_2 and when the singularity condition occurs, the integrand of I_1 becomes zero and the integrand of I_2 approaches a finite value.

Since the contour of integration is described in terms of discrete points, I_1 and I_2 can be rewritten for straight line segments connecting consecutive contour points. The equation of a line segment with unit direction vector $\vec{e}$ and starting point $\vec{y}_0$ is

$$\vec{y}(s) = \vec{y}_0 + s\vec{e}, \quad s_a < s < s_b, \quad \mathrm{d}\vec{s} = \vec{e}\,\mathrm{d}s \tag{4.10}$$

Using the following definitions

$$\vec{a} = \vec{y}_0 - \vec{z}, \quad \vec{b} = \vec{y}_0 - \vec{x}, \quad \vec{u} = \vec{a}\times\vec{b}, \quad \vec{v} = \vec{e}\times(\vec{a}-\vec{b}) \tag{4.11}$$

$$a^2 = \vec{a}\cdot\vec{a}, \quad b^2 = \vec{b}\cdot\vec{b}, \quad \alpha = \vec{a}\cdot\vec{e}, \quad \beta = \vec{b}\cdot\vec{e}, \quad \gamma = \vec{a}\cdot\vec{b} \tag{4.12}$$

the vectors $\vec{\rho}$ and $\vec{r}$ can be written in terms of s:

$$\vec{\rho} = \vec{a} + \vec{e}s, \quad \vec{r} = \vec{b} + \vec{e}s \tag{4.13}$$

$$\rho^2 = a^2 + 2\alpha s + s^2, \quad r^2 = b^2 + 2\beta s + s^2 \tag{4.14}$$

$$\vec{\rho} \cdot \vec{r} = \gamma + (\alpha + \beta)s + s^2 \tag{4.15}$$

$$(\vec{\rho} \times \vec{r}) \cdot \mathrm{d}\vec{s} = (\vec{a} \times \vec{b}) \cdot \vec{e}\,\mathrm{d}s \tag{4.16}$$

$$(\vec{\rho} \times \vec{r})^2 = (\vec{u} - \vec{v}s)^2 = \vec{u}^2 - 2\vec{u} \cdot \vec{v}s + \vec{v}^2 s^2 \tag{4.17}$$

Substituting Equations 4.13 to 4.17 into Equation 4.8, I_1 becomes

$$I_1 = \frac{e^{ikR}\vec{u} \cdot \vec{e}}{4\pi} \int_{s_a}^{s_b} \left[e^{ik(\rho + r - R)} \left(1 - \frac{\vec{\rho} \cdot \vec{r}}{\rho r} \right) - 2 \right] \frac{\mathrm{d}s}{(\vec{u} - \vec{v}s)^2} \tag{4.18}$$

Equation 4.18 is in a form that can be integrated numerically. The integrand is a piecewise continuous function of the distance along the contour of integration, s, in which the parameters $\vec{a}$ and $\vec{b}$ change as s traverses from one segment to another. The adaptive Gauss-Kronrod quadrature method in Matlab® is used because it is appropriate for oscillatory integrands.

Substituting Equations 4.13 to 4.17 into Equation 4.9, I_2 becomes

$$I_2 = \frac{e^{ikR}\vec{u} \cdot \vec{e}}{4\pi} \int_{s_a}^{s_b} \frac{2\,\mathrm{d}s}{(\vec{u} - \vec{v}s)^2} = \frac{e^{ikR} 2\vec{u} \cdot \vec{e}}{4\pi \|\vec{u} \times \vec{v}\|} \left[\tan^{-1} \frac{\vec{v} \cdot (\vec{v}s - \vec{u})}{\|\vec{u} \times \vec{v}\|} \right]_{s_a}^{s_b} \tag{4.19}$$

Furthermore, let $\vec{R} = \vec{a} - \vec{b}$, then

$$\begin{aligned} \vec{u} \times \vec{v} &= \vec{u} \times (\vec{e} \times \vec{R}) \\ &= \vec{e}(\vec{u} \cdot \vec{R}) - \vec{R}(\vec{u} \cdot \vec{e}) \\ &= \vec{e}[(\vec{a} \times \vec{b}) \cdot \vec{a} - (\vec{a} \times \vec{b}) \cdot \vec{b}] - \vec{R}(\vec{u} \cdot \vec{e}) \\ &= -\vec{R}(\vec{u} \cdot \vec{e}) \end{aligned} \tag{4.20}$$

Therefore, the final form of I_2 is

$$I_2 = \frac{e^{ikR}}{2\pi R}\left[\tan^{-1}\frac{\vec{v}\cdot(\vec{v}s-\vec{u})}{\|\vec{u}\times\vec{v}\|}\right]_{s_a}^{s_b} \tag{4.21}$$

If $\|\vec{u}\times\vec{v}\| = 0$ and the singularity condition occurs, i.e. there exists $s_a < s_0 < s_b$ such that $\vec{y}(s_0)$, $\vec{x}$, and $\vec{z}$ are colinear, then the square bracket becomes $[\frac{\pi}{2} + \frac{\pi}{2}]$ so that $I_2 = \frac{e^{ikR}}{2R}$. If $\|\vec{u}\times\vec{v}\| = 0$ and the singularity condition does not occur, i.e. there exists $s_0 < s_a$ or $s_0 > s_b$ such that $\vec{y}(s_0)$, $\vec{x}$, and $\vec{z}$ are colinear, then the square bracket becomes $[\mp\frac{\pi}{2} \pm \frac{\pi}{2}] = 0$. In both situations, $\chi = 0$.

4.4 Validation of the Diffraction Integral Method

The diffraction integral method was partially validated against NASA's Fast Scattering Code (the equivalent source method described in Section 4.1.2). Two canonical shielding geometries for the validation were proposed: a sphere and a circular disk. The flexibility of the diffraction integral method comes from the fact that it depends only on the outline of the shielding object, but this means the method cannot distinguish between objects that share the same outline. Furthermore, the derivation assumed that the outline marks a sharp transition between incident acoustic pressure on the illuminated side and zero acoustic pressure on the shadow side. Therefore, the method is expected to be more accurate for a flat shielding object characterized by edge diffracted rays than a rounded shielding object characterized by creeping rays. Comparing the diffraction integral method to the FSC for a sphere and a disk that share the same circular outline will quantity this limitation.

At this time, only the FSC results for a shielding sphere are available for validation purposes. Thus, the comparison presented here is for creeping rays only which are not well-represented by the diffraction integral method. An analytical solution for the scattering of a spherical scalar (acoustic) wave by a rigid sphere is also presented. By expanding the Helmholtz equation in spherical harmonics and imposing the boundary

conditions, one obtains: [37]

$$p_d(r,\theta) = \frac{ik}{4\pi}\sum_{n=0}^{\infty} P_n(\cos\theta) h_n^{(1)}(kr_>)\left[j_n(kr_<) - \frac{j_n'(ka)}{h_n^{(1)\prime}(ka)} h_n^{(1)}(kr_<)\right] \quad (4.22)$$

$$r_< = \min(r,\rho)$$

$$r_> = \max(r,\rho)$$

where a is the radius of the sphere, r is the distance from the center of the sphere to the observer, ρ is the distance from the center of the sphere to the source, θ is the angle between $\vec{r}$ and $\vec{\rho}$, P_n is the Legendre polynomial, j_n is the spherical Bessel function, and $h_n^{(1)}$ is the spherical Hankel function of the 1st kind. At high ka, the number of terms required for the spherical harmonics solution become impractical to compute[2]. An asymptotic solution for $ka \to \infty$ can be used instead. There are two forms of the asymptotic solution: $p_{d,S}(r,\theta)$ for inside the shadow region and $p_{d,I}(r,\theta)$ for outside the shadow region. The equations are: [37]

$$\begin{aligned} p_{d,S}(r,\theta) = & -\frac{a^{1/2}\exp\{ik[(r^2-a^2)^{1/2}+(\rho^2-a^2)^{1/2}]\}}{(8\pi kr\rho\sin\theta)^{1/2}(r^2-a^2)^{1/4}(\rho^2-a^2)^{1/4}} \\ & \cdot\sum_m \frac{\exp\left\{i\nu_m(2\pi-\theta)-\frac{i\pi}{4}\right\}+\exp\left\{i\nu_m\theta+\frac{i\pi}{4}\right\}}{1+\exp\{2\pi i\nu_m\}} \\ & \cdot\exp\left\{-i\nu_m\left[\cos^{-1}\left(\frac{a}{r}\right)+\cos^{-1}\left(\frac{a}{\rho}\right)\right]\right\}\frac{\frac{\pi e^{5\pi i/6}}{2}\left(\frac{ka}{6}\right)^{1/3}}{q_m A^2(q_m)} \end{aligned} \quad (4.23)$$

and

$$\begin{aligned} p_{d,I}(r,\theta) = & \frac{e^{ikR}}{4\pi R} + \frac{ia^{1/2}\exp\{ik[(r^2-a^2)^{1/2}+(\rho^2-a^2)^{1/2}]\}}{(8\pi kr\rho\sin\theta)^{1/2}(r^2-a^2)^{1/4}(\rho^2-a^2)^{1/4}} \\ & \cdot\sum_m \frac{\exp\left\{i\nu_m(2\pi+\theta)-\frac{i\pi}{4}\right\}+\exp\left\{i\nu_m(2\pi-\theta)+\frac{i\pi}{4}\right\}}{1+\exp\{2\pi i\nu_m\}} \\ & \cdot\exp\left\{-i\nu_m\left[\cos^{-1}\left(\frac{a}{r}\right)+\cos^{-1}\left(\frac{a}{\rho}\right)\right]\right\}\frac{\frac{\pi e^{5\pi i/6}}{2}\left(\frac{ka}{6}\right)^{1/3}}{q_m A^2(q_m)} \end{aligned} \quad (4.24)$$

where R is the distance between the source and the observer, q_m are the roots of

[2] At $ka = 370$, the spherical harmonics requires 800 terms.

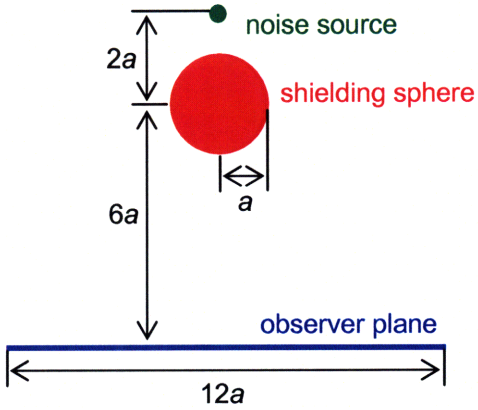

Figure 4-16: The shielding sphere configuration for the validation of the diffraction integral method

the equation $A'(q_m) = 0$, $A(x) = \int_0^\infty \cos(t^3 - xt)\,\mathrm{d}t$ is the Airy function, and $\nu_m = q_m(ka/6)^{1/3}\exp\{i\pi/3\}$. Note that the two asymptotic solutions are not continuous at the shadow boundary and the values of the solution near the shadow boundary should be disregarded.

The geometry for the shielding sphere and monopole source is shown in Figure 4-16. The comparison was made at $ka = 10$, 100, 370, 500, and 1000. The spherical harmonics analytical solution and the asymptotic analytical solution were found to overlap between $ka = 100$ and $ka = 370$. Therefore, the spherical harmonics analytical solution was used up to $ka = 370$ and the asymptotic solution was used for higher ka. The FSC results provided by NASA is available only up to $ka = 100$. The comparison is shown in Figure 4-17.

The FSC result is in agreement with the analytical solution. This is expected as the FSC is a high fidelity method. Note that the lack of oscillation in the FSC result at $ka = 100$ is due to insufficient observer density, rather than a deficiency in the code. The diffraction integral method compared reasonably well to the analytical solution. It performed best at $ka = 100$, 370, and 500. Since the diffraction integral method is a high frequency method, it is expected to be more accurate as frequency increases. This does not seem to be the case at $ka = 1000$. The hypothesis is that the diffraction integral method cannot capture creeping rays and diverges from a pure creeping ray diffraction at high frequencies. This is because the creeping ray decays as it creeps

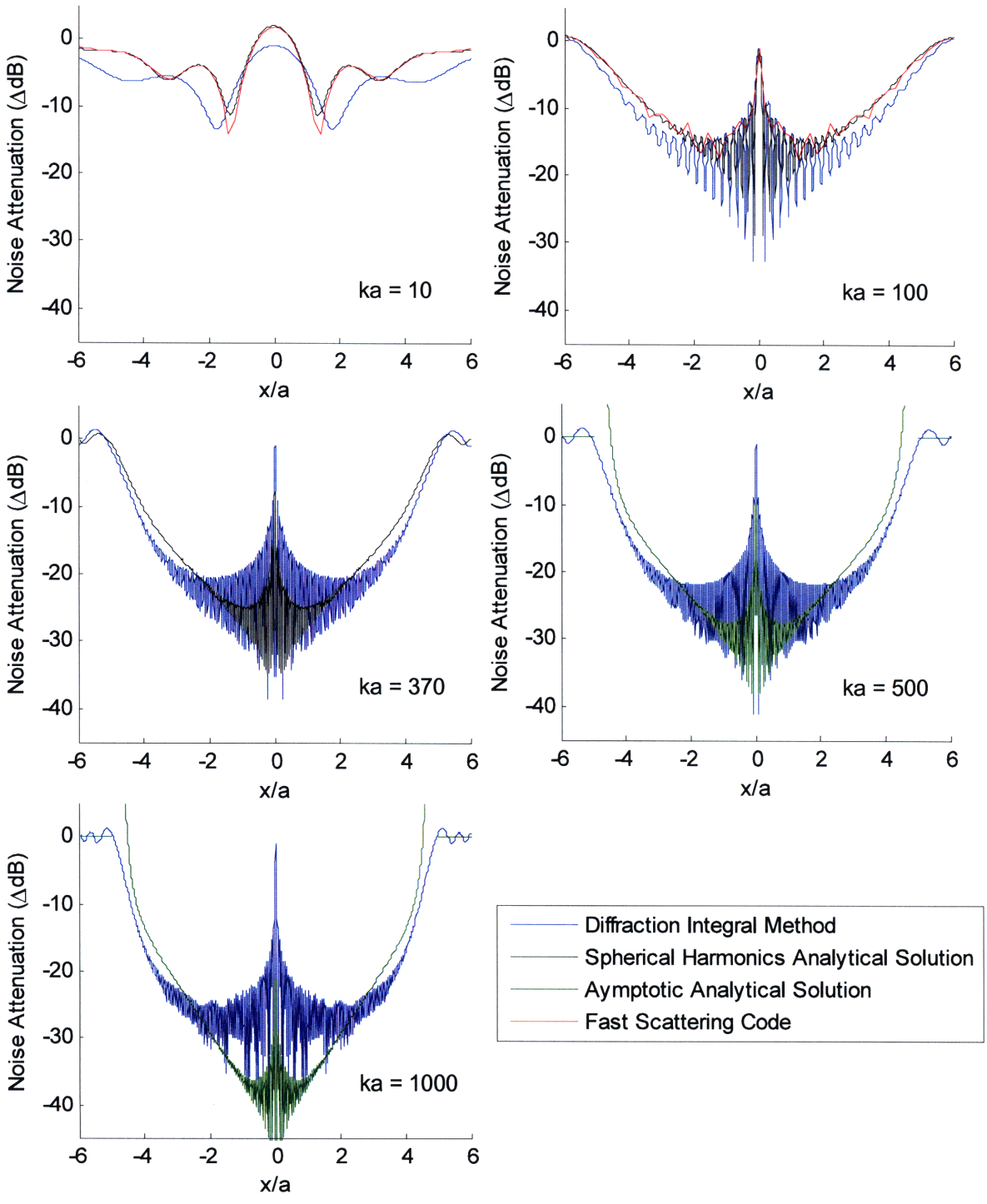

Figure 4-17: Sphere shielding comparison between diffraction integral method, analytical solution, and NASA's Fast Scattering Code

along the surface of the object at a rate that increases with frequency [37], as evident from the large amount of noise attenuation below the sphere at $ka = 1000$. This hypothesis will be tested when the FSC results for a shielding disk become available. If the diffraction integral method is in agreement with the FSC for the shielding disk at high frequencies, then the method is validated with the caveat that it performs better for a disk-like geometry than a sphere-like geometry. In practical applications, the shielding geometry will lie somewhere between the two limiting cases. The diffraction integral method is therefore expected to provide reasonable shielding estimates for an HWB airframe geometry due to its relatively flat shape and sharp trailing edges.

4.5 Acoustic Shielding Results

The diffraction integral method was applied to several aircraft geometries to demonstrate its capability and to investigate the shielding characteristics of the different aircraft configurations. In all cases, the observer plane was placed 30 m below the airframe and a single monopole source was used emitting noise at 24 center frequencies of the $\frac{1}{3}$-octave bands. The overall noise attenuation was summed over the noise attenuation for each frequency as $10 \log \left(\frac{1}{24} \sum 10^{\frac{\Delta SPL}{10}} \right)$ where ΔSPL was calculated from Equation 4.1. A comparison between the barrier shielding method, the diffraction integral method, and the ray tracing method is presented first. Next, a hypothetical 737 with engines mounted above the wings is presented followed by the N2B and N2A.

4.5.1 Comparison between Barrier Shielding, Diffraction Integral, and Ray Tracing

Noise attenuation for the SAX-20 airframe was calculated using the barrier shielding method. Straight edges were used to approximate the planform shape so that each outer wing and each half of the center body is represented by a trapezoidal plate. The trapezoidal shape is reflected in the shielding results presented in Figure 4-

18 (a). Unlike the diffraction integral method, the barrier shielding method considers each diffracting edge in isolation and is therefore unable to capture the diffraction patterns seen in Figure 4-18 (b). In addition, the barrier shielding method predicts low levels of shielding away from the centerline relative to the diffraction integral method. This suggests that the lateral EPNL for the N2A and the N2B calculated in Chapter 3 would be lower if the diffraction integral method is used in place of the barrier shielding method.

Figure 4-18 (c) shows the noise attenuation calculated with the ray tracing method by Agarwal et al. [1]. It can be seen that the diffraction integral method produced diffraction patterns similar to the ray tracing method, albeit in less detail. In particular, the red patterns near the winglets of the ray tracing results are due to creeping rays diffracting around the leading edge of the winglets. These creeping rays are not captured by the diffraction integral method and the same red patterns are not seen Figure 4-18 (b). Overall, the comparisons suggest that the diffraction integral method is a significant improvement over the barrier shielding method, but does not capture some of the high fidelity details produced by the ray tracing method.

4.5.2 Tube and Wing Shielding Prediction

A hypothetical 737-sized aircraft with the engines mounted above the wings was used to demonstrate the capability of the algorithm to obtain the aircraft outline by combining the fuselage and the wings. The outline and the noise attenuation on the observer plane are shown in Figure 4-19. The green outline indicates that the noise source above the left wing illuminates a portion of the fuselage and the wing. This is reflected in the shadow boundary that is clearly visible in the noise attenuation plot. Figure 4-19 demonstrates that the diffraction integral method is able to capture the transition from the incident region to the shadow region on the observer plane. There is about 12 dB of noise attenuation in the shadow region under the wing. However, because the conventional wing is narrow compared to the HWB planform, the shadow region is restricted to a relatively small area.

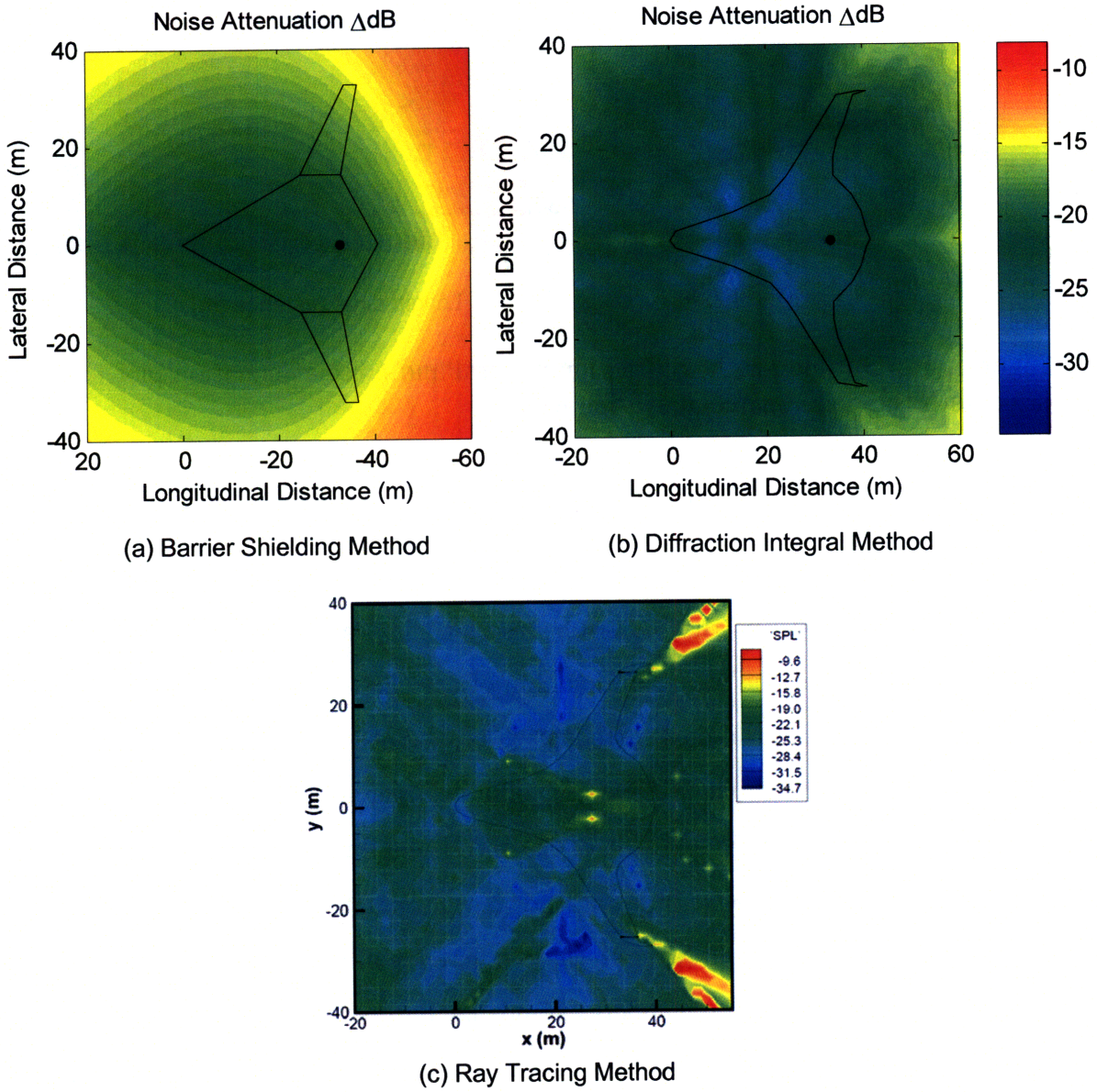

Figure 4-18: SAX-20 shielding comparison between (a) barrier shielding method, (b) diffraction integral method, and (c) ray tracing method by Agarwal et al. [1]

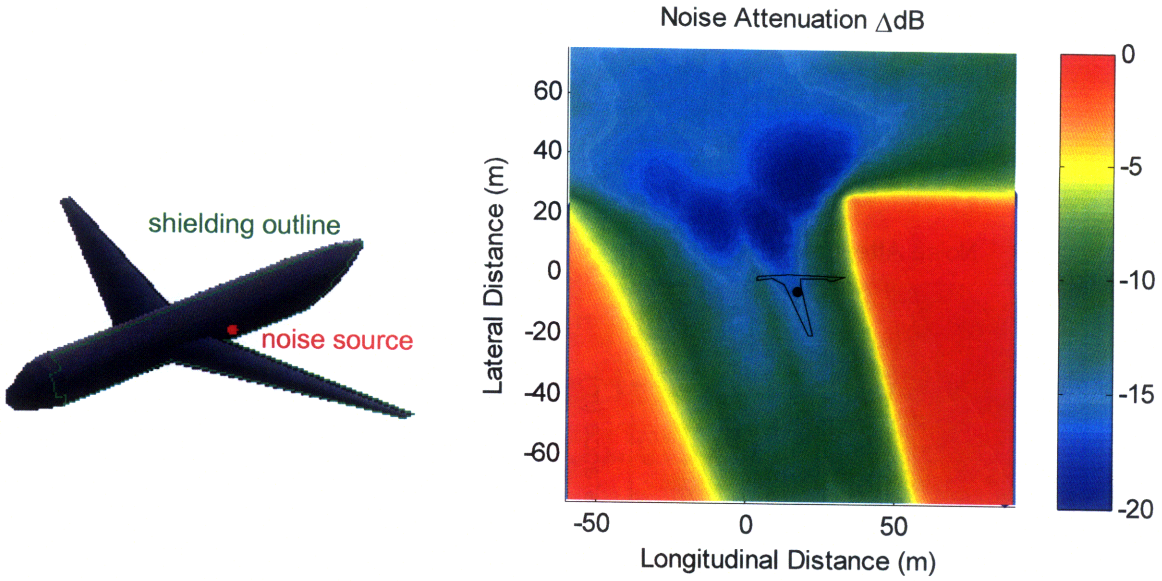

Figure 4-19: Outline for the diffraction integral and noise attenuation plot for a 737-sized with the noise source above the wing

4.5.3 N2B Shielding Prediction

The role of the N2B winglets in acoustic shielding was investigated. The airframe geometry considered was the SAX-40F described in Chapter 2. A single monopole source was placed at the mean fan location of the three engine clusters. Figure 4-20 shows the outline and the noise attenuation on the observer plane for the N2B with winglets. There is significant shielding over a larger area relative to Figure 4-19, demonstrating the shielding benefit of the HWB planform.

Figure 4-21 depicts the outline and the noise attenuation on the observer plane for the N2B without winglets. No noticeable difference in shielding was found because the shadow boundary of the winglets extends far beyond the sideline[3]. For the region of interest, i.e. centerline and sideline, the winglets have negligible effects on noise shielding. This can be seen more precisely in the line plots of noise attenuation along the centerline and the sideline in Figure 4-22.

There is about 22 dB of noise attenuation below the aircraft along both the centerline and the sideline. This is 10 dB more shielding than the tube and wing configuration. The diffraction pattern shows slightly less shielding along the centerline

[3]For 30 m altitude, the sideline is 45 m from the centerline.

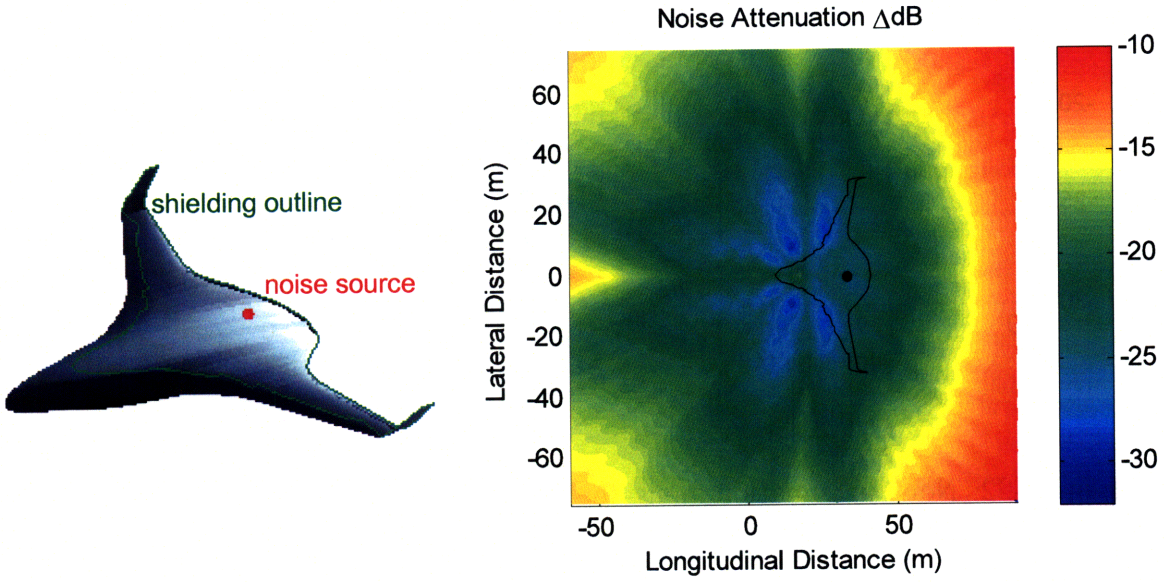

Figure 4-20: Airframe outline and noise attenuation plot for the N2B with winglets

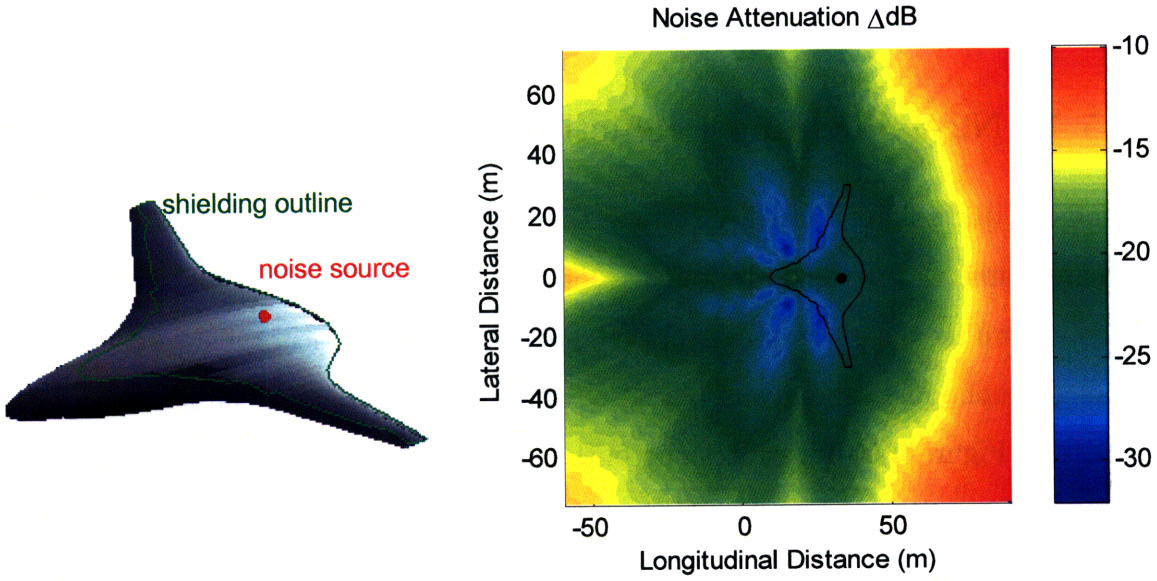

Figure 4-21: Airframe outline and noise attenuation plot for the N2B without winglets

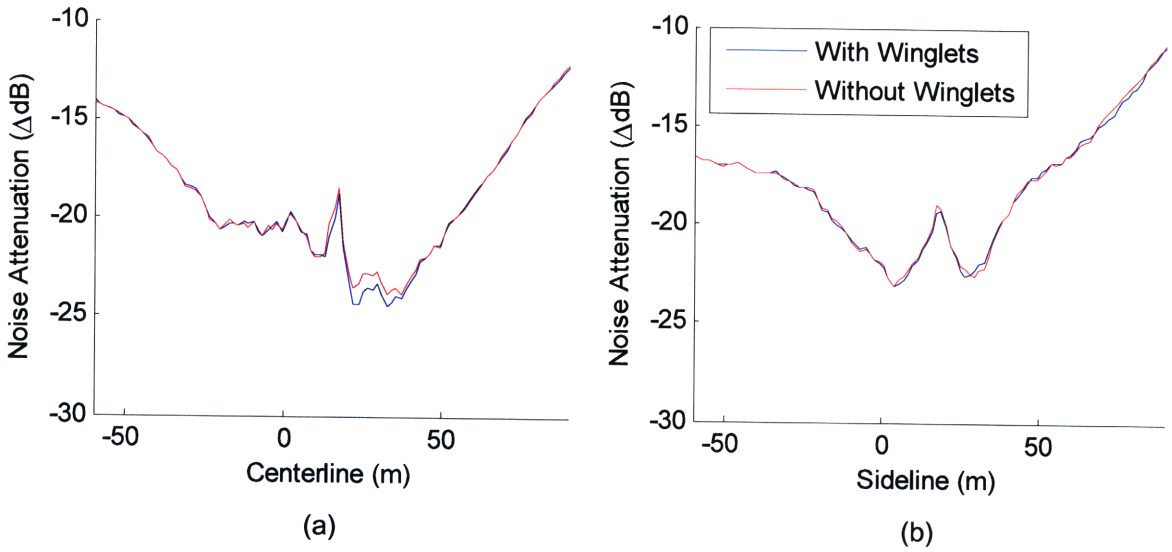

Figure 4-22: Noise attenuation along the (a) centerline and (b) sideline for the N2B

than the sideline in the forward region. The convex nature of the shielding outline at the forward portion of the center body suggests that rays from both the starboard side and the port side are diffracted towards to the centerline, increasing the sound pressure level. Conversely, the concave nature of the shielding outline between the forward portion of the center body and the outer wings results in lower sound pressure level away from the centerline.

4.5.4 N2A Shielding Prediction

Similarly, the role of the N2A vertical tails for acoustic shielding was investigated. The airframe was obtained by removing the winglets of the SAX-40F geometry and then extending the outer wings to a full span of 65 m. Vertical tails were added and a single monopole source was placed at the mean fan location of the two podded engines. Figure 4-23 illustrates the outline and the noise attenuation for the N2A with vertical tails and Figure 4-24 shows the same for the N2A without vertical tails.

The vertical tails provide a noticeable increase in shielding in the lateral direction. Unlike the winglets in the N2B, the vertical tails are close enough to the noise source to affect the noise attenuation between the centerline and the sideline. The line plots in Figure 4-25 indicate about 3 dB shielding improvement at the sideline attributed

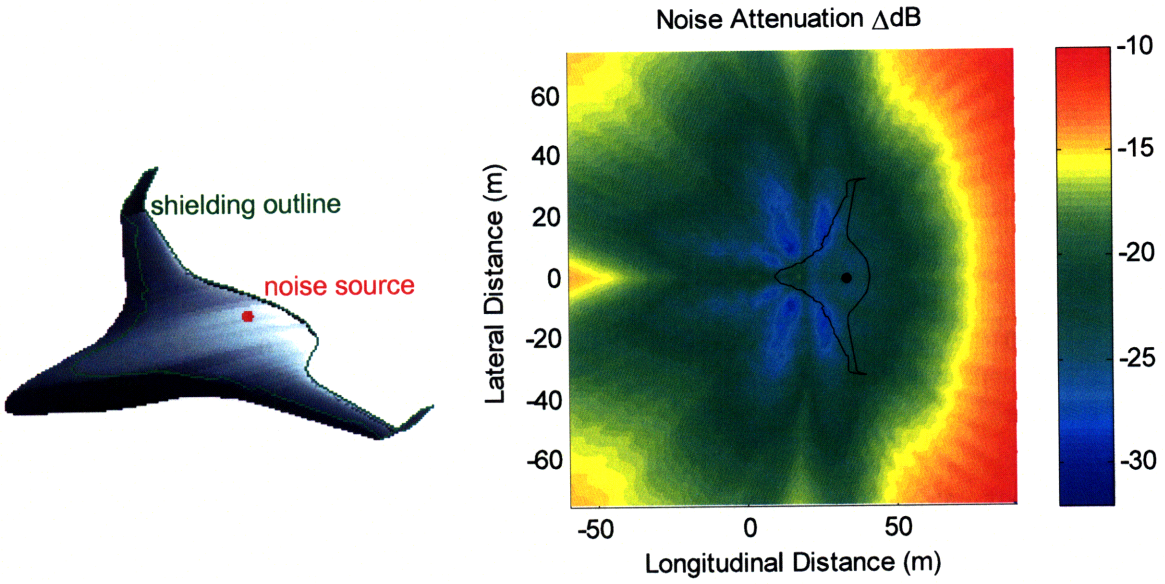

Figure 4-23: Airframe outline and noise attenuation plot for the N2A with vertical tails

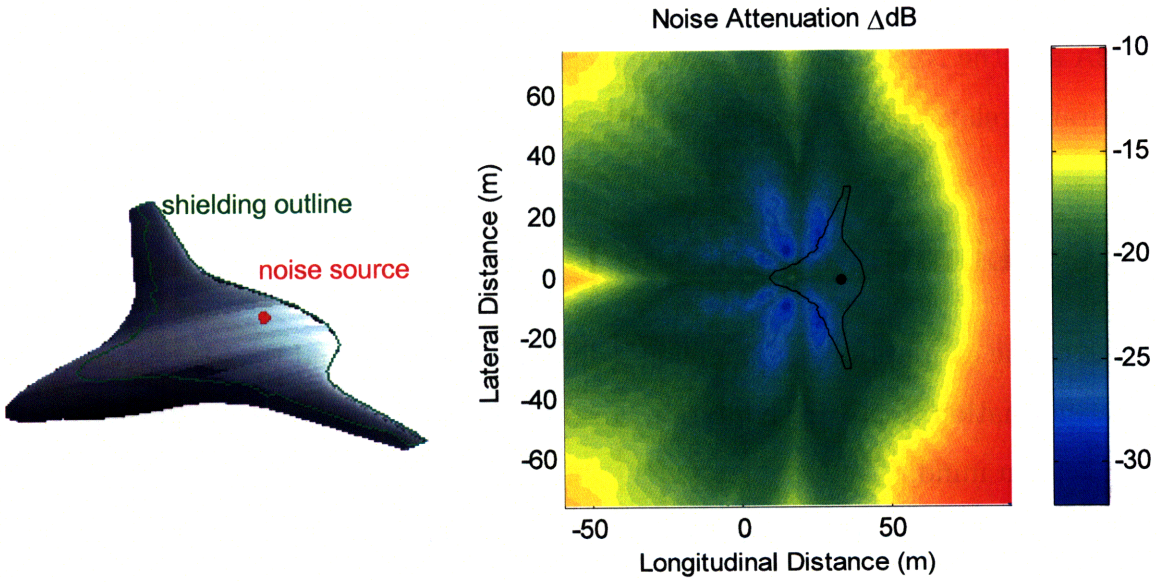

Figure 4-24: Airframe outline and noise attenuation plot for the N2A without vertical tails

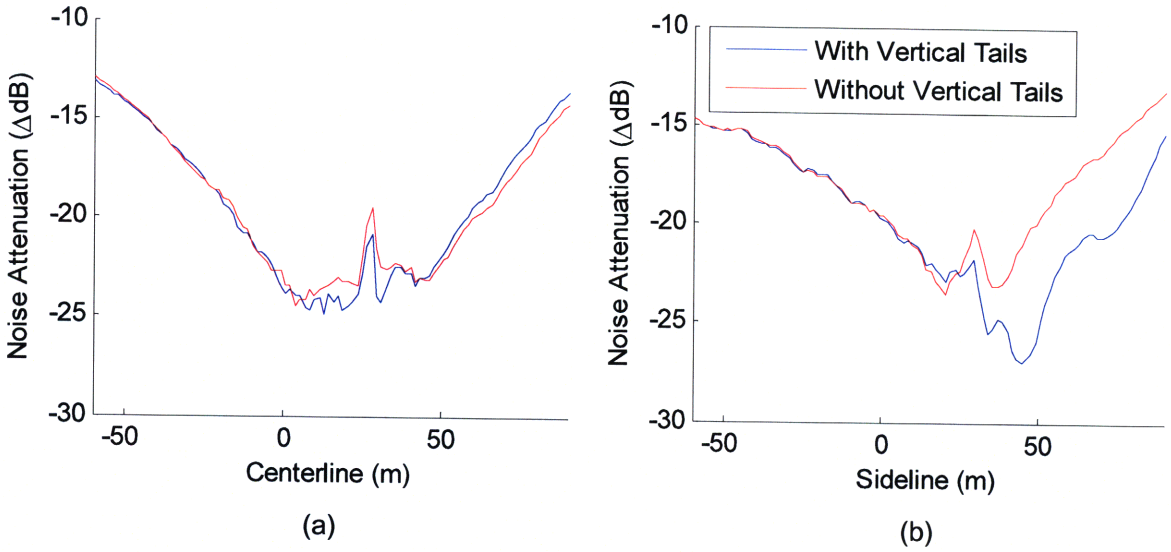

Figure 4-25: Noise attenuation along the (a) centerline and (b) sideline for the N2A

to the vertical tails.

Aside from the vertical tails, the N2A has slightly more noise attenuation than the N2B. This is because the N2A noise source is located closer towards the center of the planform than the N2B, resulting in improved shielding. This can be seen by comparing Figure 4-24 with Figure 4-21. Overall, the N2A airframe provides about 24 dB of noise attenuation, 12 dB more than the tube and wing configuration. The N2A and the N2B shielding results indicate significant low-noise benefit of the HWB airframe relative to a conventional airframe.

4.6 Limitations of the Diffraction Integral Method

Due to the assumptions in Kirchhoff's diffraction integral and the Maggi-Rubinowicz transformation, there are limitations to the diffraction integral method that need to be kept in mind.

The diffraction integral method depends only on the outline of the shielding object and does not differentiate between objects that share the same outline. Due to the formulation of the Kirchhoff diffraction integral, the diffraction integral method assumes that a sharp transition in acoustic pressure on the object surface occurs at the outline, i.e. incident pressure on the illuminated surface and zero pressure on the

shadow surface. As a consequence, the method is more accurate for shielding objects that are flat and facing the noise source. For example, the diffraction integral method for a circular outline is more applicable to a disk-like geometry characterized by edge diffracted rays than to a sphere-like geometry characterized by creeping rays.

The second key consideration is that the diffraction integral method is based on high frequency geometric acoustics. The derivation of the Kirchhoff diffraction integral assumes $ka \gg 1$; therefore, the method will not be accurate at low frequencies. Since the dominant engine frequencies are high, this does not limit the method's applicability to aircraft noise shielding. Based on the sphere diffraction results in Section 4.4, the method performed reasonably for $ka = 10$ and 100 and is expected to perform well for $ka > 370$. However, the sphere diffraction results are characterized by creeping rays rather than edge diffracted rays. A better guideline for the limiting ka value is expected after the validation for disk diffraction is completed.

The diffraction integral method does not consider reflections or multiple diffractions of the same acoustic ray. It also does not consider a moving medium. Lastly, the Maggi-Rubinowicz transformation requires the noise source to be a monopole. Source directivity can be included in the Kirchhoff diffraction integral as a multiplicative factor to the source amplitude in terms of azimuth and polar angles. However, currently the directivity factor does not allow the integral to be transformed into a simple contour integral.

Similar limitations, aside from frequency, exist for the barrier shielding method. Therefore, given its computational speed and applicability to more general geometries, the diffraction integral method is a superior to the barrier shielding method. It can be used for FAR 36 EPNL calculations where all 24 center frequencies of the $\frac{1}{3}$-octave bands are needed. If a high fidelity shielding investigation involving source directivity, moving medium, and/or a highly complex shielding geometry is required, the boundary element method, the equivalent source method, or the ray tracing method can be used instead depending on the frequency of interest.

Chapter 5

Conclusions

This thesis presented the work in support of Phase I and part of Phase II of the NASA N+2 subsonic fixed-wing project. The N2A and the N2B hybrid-wing-body aircraft were defined to meet NASA's N+2 goals in noise, fuel burn, and emissions. The aircraft noise were assessed based on FAR 36 conditions. Finally, the diffraction integral method for noise shielding prediction was implemented. The main results of the work are summarized below.

5.1 Summary of Results

The mission profile for the N+2 aircraft calls for a freighter with 103,000 lb of payload and 6000 nm range. Using the SAX-40 HWB as a baseline, two aircraft—the N2A with podded engines and the N2B with embedded engines—have been designed. In order to accommodate the new freighter mission, the interior layout and the outer wings of the SAX-40 have been modified. Despite the changes, the N2A and the N2B maintained optimal aerodynamic efficiency with elliptical lift distribution, resulting in 25% less fuel burn relative to a B767 freighter and meeting the N+2 fuel burn goal. On the other hand, FAR 36 noise estimation using ANOPP found that the N2A and the N2B are 5.7 EPNdB and 23.6 EPNdB short of the N+2 noise goal, respectively. The noise assessment showed that some noise reduction modifications to the N2A and the N2B are required. It also highlighted ANOPP's difficulty in modeling unconventional

aircraft configurations, particularly noise shielding prediction and embedded propulsion system noise prediction. Therefore, ANOPP improvements have been made with the focus in this thesis on turbomachinery noise shielding prediction.

The diffraction integral method based on previous work by Lummer [17] was developed as the improved alternative to ANOPP's current barrier shielding method. It has the advantage of being applicable to more complex geometries than the barrier shielding method yet computationally faster than the boundary element method or the ray tracing method. The idea is to numerically integrate the Maggi-Rubinowicz formulation of the Kirchhoff diffraction integral to obtain the diffracted acoustic pressure. It has been implemented in Matlab and compared to the analytical solution and the FSC results for a spherical shielding body. Application to the N2A and the N2B reveals over 20 dB of noise attenuation along the centerline and sideline from shielding. This is a significant amount of noise reduction, highlighting the benefits of the HWB planform with top-mounted engines as well as the importance of an accurate shielding prediction method for the noise assessment of unconventional configurations. The implementation of the diffraction integral method is compatible with ANOPP so that it can be integrated into ANOPP in the near future.

5.2 Key Contributions

This thesis demonstrated the advantages of the HWB aircraft configuration over the conventional tube and wing aircraft. In addition to the low fuel consumption due to its aerodynamic shape, the large planform area for engine noise shielding contributes to its low noise footprint. To analyze this advanced aircraft configuration, new tools and methods are needed. In this thesis, the diffraction integral method for turbomachinery noise shielding prediction was implemented. It is an improved-fidelity method relative to the barrier shielding method that is applicable to the HWB aircraft geometry. An advantage of the diffraction integral method is that it can be applied early on during the conceptual design phase using just an estimate of the shielding outline. When the aircraft is more developed, the full 3-D geometry may be implemented. In both cases,

the algorithm is fast enough to enable short design turnaround times, especially for FAR 36 EPNL calculations which require frequencies from 50 Hz up to 10,000 Hz.

The diffraction integral method predicted that for the N2A and the N2B aircraft configurations, vertical tails provide about an additional 3 dB shielding at the sideline whereas winglets do not affect shielding at the centerline or the sideline. Overall, the N2A and the N2B aircraft benefit from over 20 dB of noise shielding, about 10 dB more than a conventional tube and wing aircraft with engines mounted above the wings.

5.3 Recommendations for Future Work

Further noise reduction for the N2A and the N2B aircraft is needed to meet the N+2 noise goals. Modifications were suggested in Section 3.5.3, including:

- Redesign the engine cycle at a lower fan pressure ratio to reduce jet noise and fan noise.
- Employ more acoustic liners along the N2B engine ducts.
- Further development on advanced low-noise landing gear fairings.
- Mitigate elevon side edge noise with continuous mold-line or other techniques.

In addition to improvement to ANOPP's engine noise prediction for embedded propsulsion systems, other models such as undercarriage and elevons may have to be updated to incorporate these changes in the noise assessment. Aircraft performance must also be re-evaluated for changes such as the engine cycle redesign and increased acoustic liner weight in order to study the potential trade off between noise reduction and fuel burn.

Further validation of the diffraction integral turbomachinery noise shielding prediction method with the NASA's Fast Scattering Code is planned for a circular disk shielding geometry. The additional validation also serves to assess the limitation of abstracting the shielding characteristic of the object to an outline. Although the

sphere and the disk share the same outline, they produce creeping rays and edge diffracted rays, respectively. The diffraction integral method is unable to distinguish between the two objects and the comparison with FSC will quantify this deficiency. In the latter part of the N+2 project, an aerodynamic and aero-acoustic wind tunnel test is planned for the N2A and N2B. The diffraction integral method can be used to assist in determining the most informative locations for the phase arrays. Furthermore, the wind tunnel test will provide additional data to evaluate the fidelity of the diffraction integral method for a complex geometry.

Appendix A

Diffraction Integral Method User Manual

The diffraction integral method described in Chapter 4 was implemented as two main Matlab® functions. This appendix outlines the Matlab® code to calculate the noise attenuation of a shielding geometry at specified frequencies and observer locations.

A.1 File Structure

The Matlab® code is based on the two-part implementation of the diffraction integral method as described in Section 4.3. The "offline part", which determines the object outline for the contour of integration, and the "online part", which evaluates the diffraction integral to obtain the noise attenuation, were coded in separate functions. Run scripts call the two functions to predict noise attenuation for a variety of shielding geometries. The main file folder contains five files:

`CalculateShielding.m` is the function for the "online part" of the diffraction integral method. It accepts as inputs the contour of integration, source location, observer locations, and the frequencies and outputs the noise attenuation at those observer locations and frequencies. The algorithm is described in Section 4.3.2.

`FindOutline.m` is the function for the "offline part" of the diffraction integral method. It accepts as inputs the object geometry and source location and outputs the object outline. The algorithm is described in Section 4.3.1.

`RunScript_N2A.m` is the run file used to calculate the noise attenuation for the N2A. It loads the N2B geometry, modify it to the N2A geometry, and then calls the functions `FindOutline` and `CalculateShielding` in order to create a contour plot of noise attenuation on the observer plane.

`RunScript_N2B.m` is the run file used to calculate the noise attenuation for the N2B. It loads the N2B geometry and then calls the functions `FindOutline` and `CalculateShielding` in order to create a contour plot of noise attenuation on the observer plane.

`RunScript_TubeWing.m` is the run file used to calculate the noise attenuation for a conventional tube and wing aircraft. It loads the aircraft geometry and then calls the functions `FindOutline` and `CalculateShielding` in order to create a contour plot of noise attenuation on the observer plane.

The subfolder `ExampleGeometries` contains geometry files used in the run scripts for the N2A, N2B, and the conventional aircraft. The four files are:

`Geometry_N2B.mat` is the Matlab® data file containing the coordinates of the N2B geometry. The x, y, and z coordinates of the N2B airfoil sections are stored in the matrices `N2B.x`, `N2B.y`, and `N2B.z`, respectively. This file is used by `RunScript_N2A.m` and `RunScript_N2B.m`.

`Geometry_TubeWing.m` is the run file that generates the geometry of a conventional tube and wing aircraft. The fuselage is comprised of circular cross-sections and the wing is comprised of NACA 0012 airfoil sections.

`Geometry_TubeWing.mat` is the Matlab® data file containing the coordinates of the conventional aircraft generated by `Geometry_TubeWing.m`. The x, y, and z coordinates of the fuselage cross-sections are stored in the matrices `tube.x`,

`tube.y`, and `tube.z`, respectively. The x, y, and z coordinates of the wing airfoil sections are stored in the matrices `wing.x`, `wing.y`, and `wing.z`, respectively. This file is used by `RunScript_TubeWing.m`.

`naca0012.txt` is a text file containing the coordinates of a unit chord NACA 0012 airfoil. This file is used by `Geometry_TubeWing.m`.

A.2 Inputs

There are two main functions used to predict noise attenuation due to shielding, `FindOutline` and `CalculateShielding`. The inputs to the functions are described below.

A.2.1 Find Outline

The syntax for this function is

```
outline = FindOutline(density, minAngle, source, obj, orientation)
```

`density` specifies the grid density on the spherical surface for the projection of the object in terms of the number of grid points per degree longitude or latitude. The function projects the shielding object onto a sphere centered at the source and finds the outermost outline of the projection. Higher grid density produces more accurate results at a cost of longer computational time. However, computational time may also become extremely long if the grid density is too low to resolve parts of the object. There should be enough resolution to distinguish grid points inside the projected outline, on the projected outline, and outside the projected outline for all parts of the object. Furthermore, `density` must be an integer value of at least 1 point per degree.

`minAngle` is the minimum angle between the direction vectors of two consecutive outline segments. High grid density results in too many points used to define the outline. The function removes points between two outline segments when

the two segments change in direction by less than `minAngle` degrees. Increasing `minAngle` reduces the number of outline points but the outline will less closely follow the surface of the object.

`source` is a 3×1 vector containing the x, y, and z coordinates in meters of the noise source location.

`obj` is a structure of three $M \times N$ matrices, `obj.x`, `obj.y`, and `obj.z`, containing the x, y, and z coordinates in meters, respectively, that define the 3-D shielding object. The object is described by N planar cross-sections, with M points use to define each cross-section. Each cross-section is a closed contour (e.g. airfoils for wing, circles for fuselage).

`orientation` specifies the orientation of the planar cross-sections used to define the shielding object. It can have one of three possible values:

- '`x`' means cross-sections are in planes normal to the x-axis. The cross-sections are defined by the columns of `obj.y` and `obj.z`. Columns of identical values in `obj.x` specify the x locations of the cross-sections. Example: fuselage
- '`y`' means cross-sections are in planes normal to the y-axis. The cross-sections are defined by the columns of `obj.x` and `obj.z`. Columns of identical values in `obj.y` specify the y locations of the cross-sections. Example: wing
- '`z`' means cross-sections are in planes normal to the z-axis. The cross-sections are defined by the columns of `obj.x` and `obj.y`. Columns of identical values in `obj.z` specify the z locations of the cross-sections. Example: vertical tail

If the object consists of more than one component (e.g. fuselage, wing, tail), the coordinates of each component and the orientation of the cross-sections of each component may be entered separately. There is no limit, aside from computational time,

on the number of components allowed. The function finds the outermost outline for all components combined. The syntax in this case is

`outline = FindOutline(density, minAngle, source, obj1, orientation1, obj2, orientation2, obj3, orientation3, ...)`

A.2.2 Calculate Shielding

The syntax for this function is

`attn = CalculateShielding(outline, source, observer, f, ds)`

`outline` is a structure of three $1 \times P$ vectors, `outline.x`, `outline.y`, and `outline.z`, containing the x, y, and z coordinates in meters of the P points that define the outermost outline of the object. The diffraction integral is a contour integral around the outline, which divides the illuminated side and the shadow side of the shielding object.

`source` is a 3×1 vector containing the x, y, and z coordinates in meters of the noise source location.

`observer` is a structure of three $1 \times Q$ vectors, `observer.x`, `observer.y`, and `observer.z`, containing the x, y, and z coordinates in meters of the Q observer locations. The noise attenuation is calculated at each of the observer points.

`f` is a $R \times 1$ vector specifying the R frequencies in Hz of the noise source.

`ds` specifies the length in meters of the discretized outline segments. The discretization is necessary to determine if an observer lies inside or outside the shadow region. Smaller value of `ds` results in more accuracy but longer computational time. Note that the discretization has no bearing on the numerical integration; it is only for determining if the observer is inside or outside the shadow.

A.3 Outputs

The outputs of the two main functions, `FindOutline` and `CalculateShielding`, are describe below.

A.3.1 Find Outline

The syntax for this function is

```
outline = FindOutline(density, minAngle, source, obj, orientation)
```

`outline` is a structure of three $1 \times P$ vectors, `outline.x`, `outline.y` and `outline.z`, containing the x, y, and z coordinates in meters of the P points that define the object outline. If the function is unable to find a single outline, then `outline` will contain more than one element. In this case, `outline(i).x`, `outline(i).y`, and `outline(i).z` contain the coordinates of the i^{th} outline.

A.3.2 Calculate Shielding

The syntax for this function is

```
attn = CalculateShielding(outline, source, observer, f, ds)
```

`attn` is a $R \times Q$ matrix containing the noise attenuation in ΔdB at the Q observer locations and for the R frequencies.

A.4 Run Scripts

For examples on how to use the functions `FindOutline` and `CalculateShielding`, refer to the example run files `RunScript_N2A.m`, `RunScript_N2B.m`, and `RunScript_TubeWing.m`. They are set up to calculate example outputs for the noise attenuation of the N2A, N2B, and a conventional tube and wing aircraft.

The general procedure is to load the shielding object geometry, specify the source location and source frequencies, and specify the observer coordinates (an observer plane, an observer hemisphere, or just individual observer points). The script then

calls `FindOutline` to generate the object outline and use it in `CalculateShielding` to calculate noise attenuation.

Bibliography

[1] A. Agarwal, A. P. Dowling, H.-C. Shin, W. Graham, and S. Sefi, "A ray tracing approach to calculate acoustic shielding by the silent aircraft airframe," in *12th AIAA/CEAS Aeroacoustics Conference.* AIAA Paper 2006-2618, May 2006.

[2] Federal Aviation Administration, "Federal Aviation Regulations Part 36 Sec. B36.7 - Maximum Noise Levels," August 2005.

[3] D. Brown, "Airframe design," November 2007, presentation at the NASA N+2 Subsonics Fixed-Wing Project kick-off meeting.

[4] J. I. Hileman, Z. S. Spakovszky, M. Drela, and M. A. Sargeant, "Airframe design for silent aircraft," in *45th AIAA Aerospace Sciences Meeting and Exhibit.* AIAA Paper 2007-453, January 2007.

[5] R. H. Liebeck, "Blended wing body design challenges," in *AIAA/ICAS International Air and Space Symposium and Exposition: The Next 100 Years.* AIAA Paper 2003-2659, July 2003.

[6] R. H. Liebeck, "Design of the blended wing body subsonic transport," *AIAA Journal of Aircraft*, vol. 41, no. 1, pp. 10–25, January 2004.

[7] S. Wakayama and I. Kroo, "The challenge and promise of blended wing body optimization," in *7th AIAA/USAF/NASA/ISSMO Symposium on Multidisciplinary Analysis and Optimization.* AIAA Paper 1998-4736, September 1998.

[8] S. Wakayama, "Blended wing body optimization setup," in *8th AIAA/USAF/NASA/ISSMO Symposium on Multidisciplinary Analysis and Optimization.* AIAA Paper 2000-4740, September 2000.

[9] C. L. Streett, J. H. Casper, D. P. Lockard, and M. R. Khorrami, "Aerodynamic noise reduction for high-lift devices on a swept wing model," in *44th AIAA Aerospace Sciences Meeting and Exhibit.* AIAA Paper 2006-212, January 2006.

[10] F. V. Hutcheson, T. F. Brooks, and W. M. Humphreys Jr., "Noise radiation from a continuous mold-line link flap configuration," in *14th AIAA/CEAS Aeroacoustics Conference.* AIAA Paper 2008-2966, May 2008.

[11] M. G. Smith, B. Fenech, L. C. Chow, N. Molin, W. Dobrzynski, and C. Seror, "Control of noise sources on aircraft landing gear bogies," in *12th AIAA/CEAS Aeroacoustics Conference.* AIAA Paper 2006-2626, May 2006.

[12] W. Dobrzynski, B. Schning, L. C. Chow, C. Wood, M. Smith, and C. Seror, "Design and testing of low noise landing gears," in *11th AIAA/CEAS Aeroacoustics Conference.* AIAA Paper 2005-3008, May 2005.

[13] M. Herr and W. Dobrzynski, "Experimental investigations in low-noise trailing edge design," *AIAA Journal*, vol. 43, no. 6, pp. 1167–1175, June 2005.

[14] A. Agarwal and A. P. Dowling, "The calculation of acoustic shielding of engine noise by the silent aircraft airframe," in *11th AIAA/CEAS Aeroacoustics Conference.* AIAA Paper 2005-2996, May 2005.

[15] L. L. Beranek, *Noise and Vibration Control.* NY: McGraw-Hill Book Company, 1971, pp. 174–180.

[16] Z. Maekawa, "Noise reduction by screens," in *Applied Acoustics.* Elsevier Publishing Company Ltd., 1968, pp. 157–173.

[17] M. Lummer, "Maggi-rubinowicz diffraction correction for ray-tracing calculations of engine noise shielding," in *14th AIAA/CEAS Aeroacoustics Conference.* AIAA Paper 2008-3050, May 2008.

[18] J. I. Hileman, Z. S. Spakovszky, and M. Drela, "Aerodynamic and aeroacoustic three-dimensional design for a silent aircraft," in *44th AIAA Aerospace Sciences Meeting and Exhibit.* AIAA Paper 2006-241, January 2006.

[19] A. P. Plas, M. A. Sargeant, V. Madani, D. Crichton, E. M. Greitzer, T. P. Hynes, and C. A. Hall, "Performance of a boundary layer ingesting (BLI) propulsion system," in *45th AIAA Aerospace Sciences Meeting and Exhibit.* AIAA Paper 2007-450, January 2007.

[20] D. Crichton, E. de la Rosa Blanco, T. Law, and J. I. Hileman, "Design and operation for ultra low noise take-off," in *45th AIAA Aerospace Sciences Meeting and Exhibit.* AIAA Paper 2007-456, January 2007.

[21] A. R. Jones, "Multidisciplinary optimization of aircraft design and takeoff operations for low noise," Master's thesis, Massachusetts Institute of Technology, May 2006.

[22] S. F. Hoerner, *Fluid-Dynamic Drag.* NJ: Hoerner Fluid Dynamics, 1965.

[23] D. P. Raymer, *Aircraft Design: A Conceptual Approach*, 3rd ed. VA: American Institute of Aeronautics and Astronautics, September 1999, p. 473.

[24] J. Rams, "Thrust vectoring nozzle weight," June 2006, personal communication to James Hileman.

[25] S. Wakayama, "Multidisciplinary design optimization of the blended- wing-body," in *7th AIAA/USAF/NASA/ISSMO Symposium on Multidisciplinary Analysis and Optimization.* AIAA Paper 1998-4938, September 1998.

[26] P. Weed, Master's thesis in progress, Massachusetts Institute of Technology, expected 2009.

[27] Federal Aviation Administration, "Federal Aviation Regulations Part 36 Sec. B36.3 - Reference Noise Measurement Points," August 2002.

[28] Federal Aviation Administration, "Federal Aviation Regulations Part 36 Sec. B36.7 - Noise Certification Reference Procedures and Conditions," August 2002.

[29] T. F. Brooks and M. A. Marcolini, "Airfoil tip vortex formation noise," *AIAA Journal*, vol. 24, no. 2, pp. 246–252, February 1986.

[30] A. P. Dowling and J. E. Ffowcs-Williams, *Sound and Sources of Sound.* Ellis Horwood Limited, 1983.

[31] A. Manneville, D. Pilczer, and Z. S. Spakovszky, "Preliminary evaluation of noise reduction approaches for a functionally silent aircraft," *AIAA Journal of Aircraft*, vol. 43, no. 3, pp. 836–840, May 2006.

[32] J. E. Ffowcs-Williams and L. H. Hall, "Aerodynamic sound generation by turbulent flow in the vicinity of a scattering half plane," *Journal of Fluid Mechanics*, vol. 40, no. 4, pp. 657–670, 1970.

[33] M. H. Dunn and A. F. Tinetti, "Aeroacoustic scattering via the equivalent source method," in *10th AIAA/CEAS Aeroacoustics Conference.* AIAA Paper 2004-2937, May 2004.

[34] C. A. Reimann, A. F. Tinetti, and M. H. Dunn, "Noise prediction studies for the blended wing body using the fast scattering code," in *11th AIAA/CEAS Aeroacoustics Conference.* AIAA Paper 2005-2980, May 2005.

[35] J. R. P. van Rens, B. J. E. van Rens, T. van Holten, and G. J. J. Ruijgrok, "Sound level predictdion using a ray tracing algorithm for a blended wing body," in *6th AIAA/CEAS Aeroacoustics Conference.* AIAA Paper 2000-2069, June 2000.

[36] A. Sommerfeld, *Optics*, ser. Lectures on Theoretical Physics. London: Academic Press Inc., 1954, vol. 4.

[37] B. R. Levy and J. B. Keller, "Diffraction by a smooth object," *Communications on Pure and Applied Mathematics*, vol. 12, pp. 159–209, 1959.